Hindawi
Advances in Materials Science and Engineering
Volume 2022, Article ID 3992402, 22 pages
https://doi.org/10.1155/2022/3992402

Research Article

Electromagnetic Interference Shielding and Characterization of Ni^{2+} Substituted Cobalt Nanoferrites Prepared by Sol-Gel Auto Combustion Method

Rezhna Kuekha,[1] **Tahseen H. Mubarak**,[2] **and Bruska Azhdar**[3]

[1]*Department of Physics, College of Education, Garmian University, Kalar, Iraq*
[2]*Department of Physics, College of Education, Diyala University, Diyala, Iraq*
[3]*Nanotechnology Research Laboratory, Department of Physics, College of Science, University of Sulaimani, Sulaimani, Iraq*

Correspondence should be addressed to Bruska Azhdar; bruska.azhdar@univsul.edu.iq

Received 24 September 2022; Revised 25 October 2022; Accepted 14 November 2022; Published 28 November 2022

Academic Editor: Hom Kandel

The structural, magnetic, and dielectric properties of a series of Ni^{2+} substituted cobalt nanoferrite particle samples with the composition $Co_{1-x}Ni_xFe_2O_4$ (where $x = 0.0 \leq x \leq 1.0$) synthesized by using the sol-gel auto combustion route are presented in this report. The electromagnetic interference shielding of $Co_{1-x}Ni_xFe_2O_4$/PVA nanocomposite films has been determined in the microwave X-band (8.2–12.4 GHz) frequencies. X-ray analysis revealed the single-phase formation of nickel-substituted cobalt nanoferrite samples. The decreasing trend of lattice parameters with Ni^{2+} substitution indicates the incorporation of Ni^{2+} into the crystal structure, obeying Vegard's law. FTIR showed the absorption bands at 560–590 cm^{-1} (ν_1) and 390–400 cm^{-1} (ν_2) were attributed to (*A*-site) tetrahedral and (*B*-site) octahedral groups complex, respectively which confirm the spinel structure of the samples. Field emission scanning electron microscopy showed agglomerated grains of different sizes and shapes in the morphological observation. EDS reveals the chemical composition of the prepared samples. TEM analysis revealed that the synthesized particles were nearly monodisperse, show to be roughly spherical in shape, and have a polycrystalline nature. The dielectric constant and loss tangent ($\tan\delta$) is found to decrease with increasing frequency which shows normal behavior for ferrimagnetic materials. The magnetic properties determined using VSM have substantially changed with the substitution of Ni^{2+} ions. The saturation magnetization and the experimentally magnetic moment are observed to decrease with an increase in Ni^{2+} content *x*. A series of $Co_{1-x}Ni_xFe_2O_4$/PVA nanocomposite films are prepared by applying simple, rapid, and inexpensive methods for EMI shielding materials. The vector network analyzer data were used to evaluate the electromagnetic interference (EMI) shielding properties of the $Co_{1-x}Ni_xFe_2O_4$/PVA samples. At 9.2 GHz, a study of reflection loss showed a minimum reflection loss (RL) of −32.08 dB. Also, the synthesized $Co_{1-x}Ni_xFe_2O_4$/PVA nanocomposite samples show improved performance for EMI efficiency which proves the utility of this doping. With this low RL value, the results and techniques also promise a simple, effective approach to achieve light-weight $Co_{1-x}Ni_xFe_2O_4$/PVA nanocomposite films and make it excellent microwave absorbers, capable of working at gigahertz frequencies for application potentials in EMI shielding material, communication, radar stealth technology, and electronic warfare.

1. Introduction

Ferrite is produced by mixing metallic elements including cobalt (Co), barium (Ba), magnesium (Mg), nickel (Ni), manganese (Mn), and zinc (Zn), in small amounts with iron oxide (Fe_2O_4) in large amounts [1]. The general chemical formula for spinel ferrites is MFe_2O_4 where *M* is the divalent metallic ion. The characteristic of spinel ferrites can be changed by substituting a different metal ion.

The synthesis and characterization of nanoferrite particles are taking great interest due to their wide range of applications in many areas such as electrical [2], electronic

[3], magnetic [4], and microwave absorption [5–8], and their outstanding properties such as the large surface area to volume ratio, high magnetic permeability, and high saturation magnetization [9].

With the massive development of electronic science technologies, communication systems, and electronic equipment and products, one of the novel kinds of environmental pollution called the problem of electromagnetic interference (EMI) which is electromagnetic radiation blocking by conducting or magnetic barrier materials has become more significant [10, 11]. Electromagnetic radiation emitted from electronic and electrical devices such as laptops, phones, and computers results in such pollution. Electromagnetic interference (EMI) causes a serious risk to human health as well as generates electronic system interruption due to the heat from advanced electronic materials [12, 13]. The EM noise of any frequency range can be produced by an EMR. As a result, there has been growing research interest in inventing and developing novel forms of electromagnetic absorption and shielding materials. These shielding nanomaterials because of their ability to suppress interference radiation have been widely used in numerous fields of aerospace systems as well as communication [14, 15]. Because of their good chemical stability, high saturation magnetization, and good matching for magnetic and dielectric properties, ferrite materials such as Co, Mn, Zn, and Ba are getting more and more popular among the various candidates for EMI shielding [16–18].

The mechanism of EMI shielding happens when EMR interacts on the shielding surface according to Lorentz's force law and to form the EM field the electrons of the shielding material interact with the incident EMR. The induced field moves in the opposite direction as the incident EM waves. The incident EM radiation energy causes the induced EMR to decrease. The characteristics that contribute to the shielding process are absorption, reflection, and multiple reflections [19]. Based on their shielding principles different kinds of shielding are present such as magnetic field shielding, electric field shielding, and EM field shielding. The basic purpose of shielding is to block the entrance of EM waves [20, 21]. The charge of the conductor surface is rearranged in the field of external electrostatic discharge to attain the field until the conductor reaches zero strength, which is the primary mechanism of electrostatic shielding. Metals provide excellent EMI shielding due to their electrical properties. Magnetic field shielding works by suppressing radiation from the external magnetic field, which is a low-frequency field. Increasing the nanomaterials permeability value results in a magnetic flux loop toward the magnetic resistance causing the magnetic resistance to decrease. Ferromagnetic materials for low-frequency magnetic fields are good nanomaterials [22, 23].

In this study, the effect of Ni^{2+} substitution on the structural, magnetic, and dielectric characteristics of cobalt nanoferrite particles is reported in detail. The nanocomposite based on polyvinyl alcohol and Ni^{2+} substituted cobalt nanoferrite particles are synthesized and tested to study shielding against the interference caused by EMI signal in the frequency range of X-band (8.2–12.4 GHz) was discussed in detail.

2. Chemicals and Reagents

Analytical grade chemicals and reagents from Honeywell/Fluka and Biochem Chemopharma were obtained. These materials were used for the synthesis of Ni^{2+} substituted cobalt spinel nanoferrite particles with the composition of $Co_{1-x}Ni_xFe_2O_4$ (where $x = 0.0 \leq x \leq 1.0$) without further purification. Cobalt (II) nitrate hexahydrate ($Co(NO_3)_2.6H_2O$), nickel (II) nitrate hexahydrate ($Ni(No_3)_2.6H_2O$), and iron (III) nitrate nonahydrate ($Fe(NO_3)_3.9H_2O$) were used as a metal ion source. Citric acid monohydrate ($C_6H_8O_7.H_2O$) acts as a chelating agent (fuel) and helps in the homogeneous distribution of metal ions. Dilute ammonia (NH_3) is used to maintain the solution neutral pH ~ 7. Ultrapure water (Milli-Q grade, 18 $M\Omega{\cdot}cm^{-1}$) is used during the experimentation for the synthesis of the materials. Details of chemicals and reagents are provided in Table 1.

3. Experimental Procedures

The experimental procedures are described in the following sections.

3.1. Synthesis of $Co_{1-x}Ni_xFe_2O_4$ Nanoparticles. Using the sol-gel autocombustion approach [24], nanocrystalline Ni^{2+} substituted cobalt nanoferrite of the chemical composition $Co_{1-x}Ni_xFe_2O_4$ (where $x = 0.0 \leq x \leq 1.0$) is synthesized as shown in Figure 1. By dissolving the desired proportions of cobalt (II) nitrate, nickel (II) nitrate, and iron (III) nitrate in ultrapure water, citric acid acts as an organic fuel during the calcination process and chelating agent for metal ions in sol-gel auto combustion in preparation of many oxides. Citric acid is separately dissolved in ultrapure water in a separate beaker. The molar ratio of metal nitrate ions to citric acid was 3 : 2.2. After completely mixing the two solutions by using ultrasonic for 10 minutes, continual stirring was carried out until the temperature reached 50°C and remained at this temperature for 30 minutes. After that, dilute ammonia was added dropwise to the solution to attain a pH of 7. The temperature was then raised to 90°C. The obtained solution was transformed into a viscous brown gel phase. The viscous gel was placed in an oven at 200°C to initiate an autocombustion reaction and produce a fluffy powder and dried in an oven for 30 minutes. The prepared fluffy powder was ground and the obtained as-burnt powders of $Co_{1-x}Ni_x2e_2O_4$ (where $x = 0.0 \leq x \leq 1.0$) nanoferrites particles after combustion were calcinated in a programmed muffle furnace at 600, 700, and 800°C for 3 hours to get rid of organic waste and to obtain the homogeneity; then, it was used for further investigation of structural, magnetic, and dielectric properties.

3.2. Pelletizing and Nanocomposite Preparation. A small amount of (2 wt%) PVA was added as a binder to the samples that were calcinated at 800°C before being pressed into circular pellets with a diameter of 12 mm and a thickness of around 2 mm using a hydraulic press at a

Table 1: Chemicals and reagents.

Reactant	Chemical formulae	Molar mass	Role	Supplier
Cobalt (II) nitrate	$Co(NO_3)_2.6H_2O$	291.04	Metal ion source	Honeywell/fluka
Nickel (II) nitrate	$Ni(No_3)_2.6H_2O$	290.81	Metal ion source	Biochem chemopharma
Iron (III) nitrate	$Fe(NO_3)_3.9H_2O$	404.06	Metal ion source	Honeywell/fluka
Citric acid	$C_6H_8O_7.H_2O$	210.14	Fuel (chelating agent)	Biochem chemopharma
Ammonia	NH_3		pH controller	Biochem chemopharma
Ultrapure water (milli-Q grade, 18 MΩ·cm^{-1})	H_2O	18.02	Reaction medium	

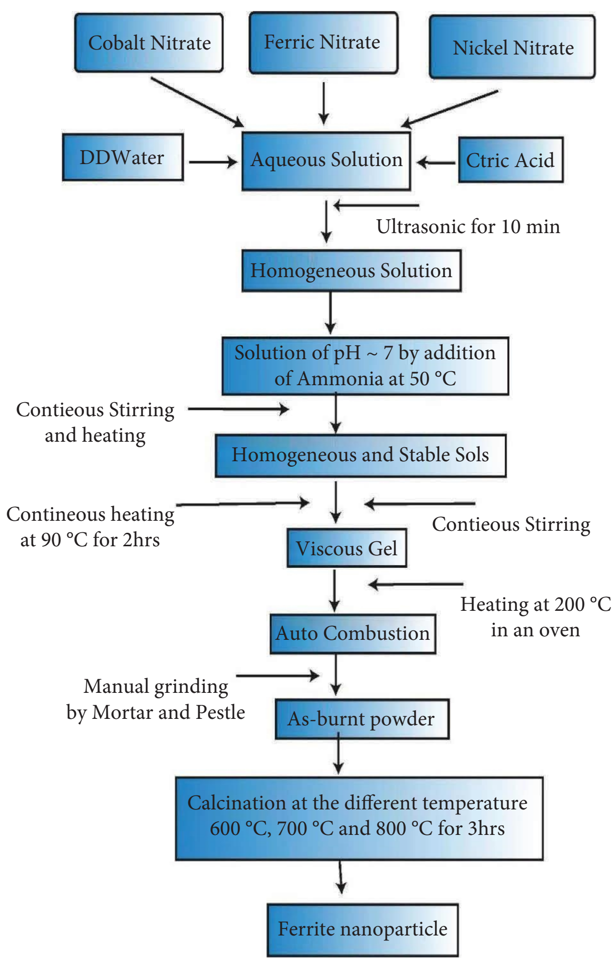

Figure 1: Schematic representation of the sol-gel autocombustion method for the $Co_{1-x}Ni_xFe_2O_4$ (where $x = 0.0 \leq x \leq 1.0$).

pressure of 5 tons for 5 minutes. The prepared pellets were then sintered at 900°C for 3 hours to densify the samples and remove the excess binder. Slowly it is allowed to cool naturally to evaluate the dielectric characteristics.

The solution casting route is used for the preparation of a series of PVA-nanocomposite films with a 10% weight of $CoFe_2O_4$, $Co_{0.6}Ni_{0.4}Fe_2O_4$, and $NiFe_2O_4$ nanoferrite particle samples. The representative picture of the produced $Co_{1-x}Ni_xFe_2O_4$/PVA nanocomposite sample is shown in Figure 2. Typically, 1 gm of PVA was added to 40 ml of water under continuous stirring at 80°C. Then, 10% weight of the prepared nanoferrite particles is dispersed in ultrapure water separately and sonicated for one hour. Then, after sonicating for one hour, the nanoferrite solution was added to the PVA solution to obtain the required composition. After that, each sample was sonicated for one hour separately. Then, the resultant solution was poured into a petri dish after complete dispersion and left at room temperature for 48 hours to dry. Samples were termed as PF1, PF2, and PF3.

4. Results and Discussion

Results and discussion are discussed in the following sections.

4.1. Crystallographic Analysis. High-intensity X-ray diffraction (XRD, model Panalytical (X'pert Pro, Netherlands)) equipped with a copper-kα radiation source (with an incident X-ray wavelength of $\lambda = 0.154$ nm, 40 mA, 40 kV) confirmed the successful fabrication, crystal structure, and phase identification of the synthesized as-burnt and calcined samples with the composition $Co_{1-x}Ni_xFe_2O_4$ (where $x = 0.0 \leq x \leq 1.0$), all measurements were taken in increments of 0.026° in the 2θ range (20°–70°). Figure 3 shows the X-ray diffraction pattern of the $Co_{1-x}Ni_xFe_2O_4$ (where $x = 0.0 \leq x \leq 1.0$) nanoferrite particles for as-burnt and calcinated at 600°C, 700°C, and 800°C.

Calcination was carried out to remove any external phases and reduce internal stress, the size of the $Co_{1-x}Ni_xFe_2O_4$ (where $x = 0.0 \leq x \leq 1.0$) nanoparticles also increase which led to crystal growth prepared nanoparticles. All the samples were found to be face-centered cubic (FCC) with an Fd-3m space group. According to the standard ICSD cards [00-001-1121] and [00-010-0325], the product can be mainly indexed with the miller indices of the reflection planes of (111), (220), (311), (222), (400), (422), (511), and (440), which can be indexed to $CoFe_2O_4$ and $NiFe_2O_4$ respectively, and this pattern was also confirmed with previously published data [25–27]. These diffraction peaks confirmed the formation of nanometer-sized particles, and the substitution of the spinel crystal structure. The XRD result indicates both high crystallinity and purity of the $Co_{1-x}Ni_xFe_2O_4$ (where $x = 0.0 \leq x \leq 1.0$) nanoparticles samples.

The peak attributed to the (311) plane has the highest peak intensity, and it changes to a higher diffraction angle when nickel substitution in cobalt ferrites increases. The shifting of the (311) peak towards higher 2theta angles, which indicates a drop in lattice constant with Ni^{2+} substitution, is clearly shown in Figure 4. The result might be due to the difference in ionic radii of Ni^{2+} (0.69 Å) ion and Co^{2+} (0.745 Å) ion.

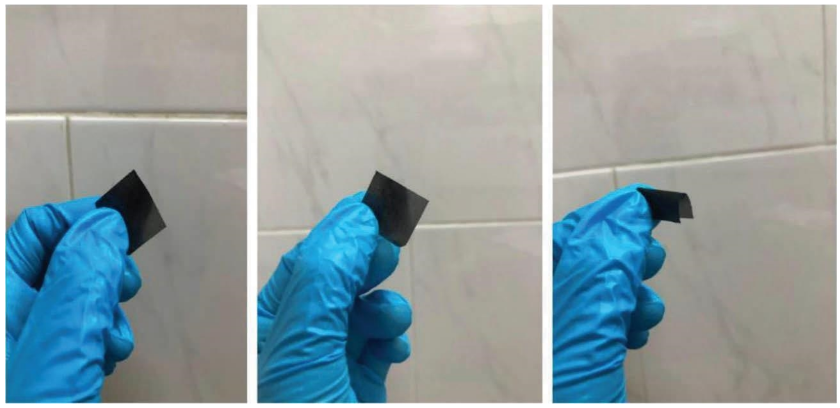

Figure 2: The representative picture of the produced $Co_{1-x}Ni_xFe_2O_4$/PVA nanocomposite sample.

The lattice parameter "a" can be determined using the following relation in the case of cubic crystal structure [28]:

$$\frac{1}{d_{hkl}^2} = \frac{h^2 + k^2 + l^2}{a^2},$$
$$V = a^3, \tag{1}$$

where d is the interplanar spacing and h, k, and l are the miller indices of the crystal planes. Figure 5 shows that the lattice parameter value decreases linearly with nickel concentration, which can be described by the decreased ionic radius of Ni^{2+} compared to Co^{2+} this variation can be explained by Vegard's law [29]. The unit cell dimensions of pure nickel ferrites and pure cobalt ferrites are quite similar to the values obtained in this report.

Because of the smaller crystallite size, the peak intensity decreases as nickel substitution increases from $x = 0.0$ to $x = 1.0$. From the most intense peak (311), the average crystallite size of the prepared $Co_{1-x}Ni_xFe_2O_4$ (where $x = 0.0 \le x \le 1.0$) nanoferrite particles were calculated using the Scherrer formula [30].

$$D = \frac{k\lambda}{\beta \cos\theta}, \tag{2}$$

where D represents the average crystallite size, k corresponds to the Scherrer constant (0.90), β is the full width at half-maximum, λ is the radiation wavelength of the X-ray, and θ is the diffraction angle corresponding to (311) plane, respectively. This method produces nano-crystals with a size of 49–65 nm, which is suitable for practical applications such as wireless communication, electronic warfare, radiation medical exposure, sensing, and aerospace that need small-volume, light, and very efficient screening systems to protect a specific component and its surroundings [31]. The peaks in the XRD pattern for all the samples get sharper and narrower when the calcined temperature increases to 800°C, with a decrease in their FWHM (full width at half maxima). This shows that crystallinity and particle size have increased. The observed behavior indicates that the present samples have nanocrystalline nature. It is detected that with the calcined temperature the particle size also increases as shown in Figure 6.

Calcining the samples will increase the crystallinity. By increasing the temperature, the estimated average crystallite size increases so, particle size and grain size will increase and the dominant peak shape becomes sharper by calcining because the same wavelength is hitting one particle instead of hitting small particles of the same orientation. Additionally, we observed a decrease in the FWHM which is a narrowing of the peaks corresponding to an increase in crystallization of the nano-materials with calcination temperature, if full width at half maximum decreases, which means that the crystallinity also increases [32, 33].

Since each primitive unit cell of the spinel structure contains 8 molecules, the value of the X-ray density ρ_x was calculated according to [34]

$$\rho_x = \frac{8M}{Na^3}, \tag{3}$$

where M represents the molecular weight of the sample, N is Avogadro's number (= $6.0225 * 10^{23}$ atom/mole), and a is the experimental lattice parameter. The measured X-ray density is tabulated in Table 2. With increasing the nickel concentration, X-ray density also increases as in Figure 5, subsequently, the cobalt atom is lighter than the nickel atom. The bulk density ρ_b was calculated from the following formula [35]:

$$\rho_b = \frac{m}{\pi r^2 d}, \tag{4}$$

where r is the radius, m is the mass, and d represents the thickness of the sample. The obtained results are tabulated in Table 2.

Because of the existence of pores in the sample formed during the synthesis process, which is further characterized by the term porosity, bulk density is often lower than X-ray density, and the percentage bulk porosity of the sample was estimated using the following relation [36]:

$$P = \left(1 - \frac{\rho_b}{\rho_x}\right) * 100. \tag{5}$$

There is an inverse relationship between bulk porosity and bulk density.

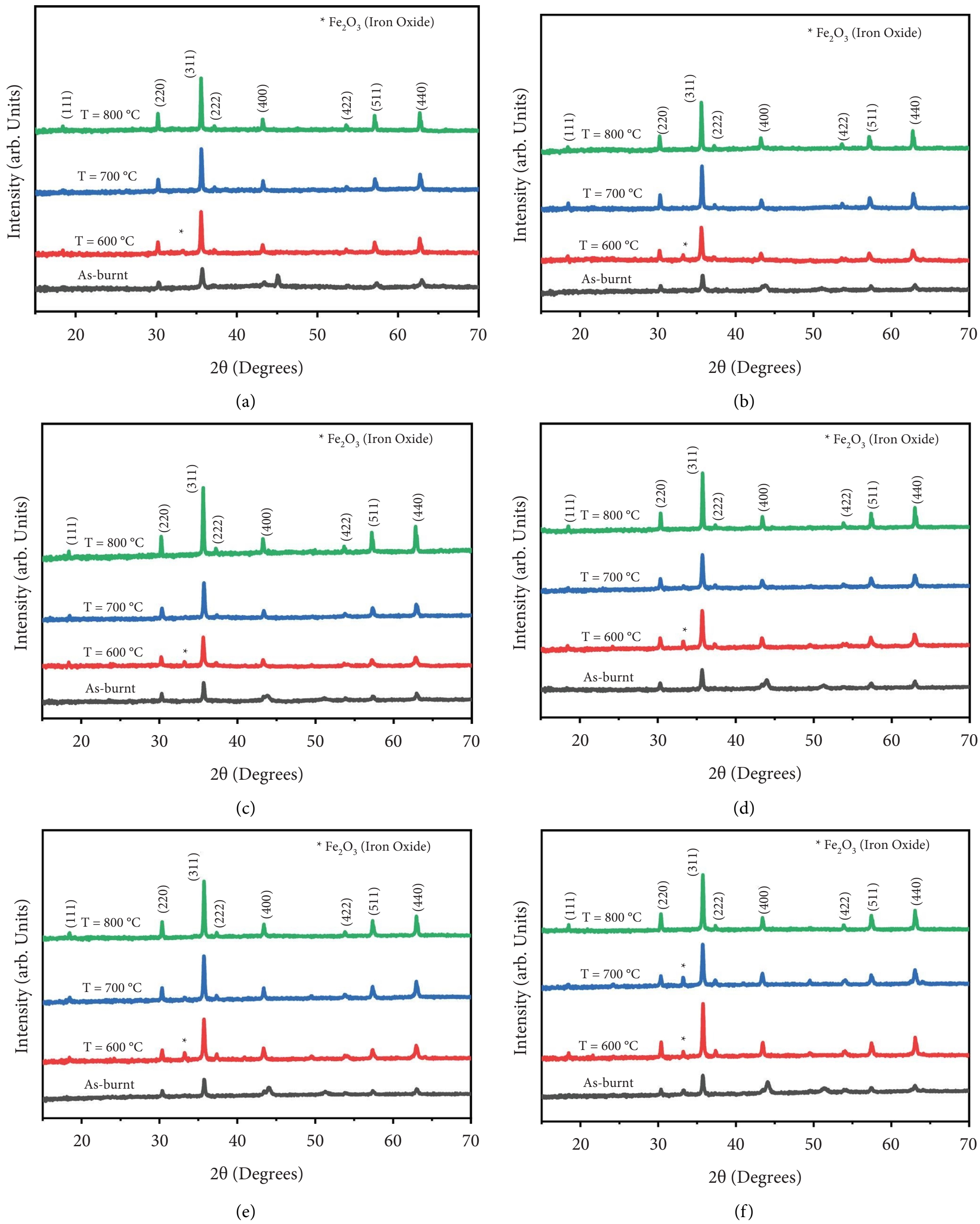

Figure 3: Nanoferrite particles X-ray diffraction pattern of (a) $CoFe_2O_4$, (b) $Co_{0.8}Ni_{0.2}Fe_2O_4$, (c) $Co_{0.6}Ni_{0.4}Fe_2O_4$, (d) $Co_{0.4}Ni_{0.6}Fe_2O_4$, (e) $Co_{0.2}Ni_{0.8}Fe_2O_4$, and (f) $NiFe_2O_4$.

The ferrite systems' physical properties are influenced by hopping length L; the distance between the magnetic ions, the hopping length in A-site (L_A-tetrahedral) and B-site (L_B-octahedral) were estimated using the following equations [37]:

$$L_A = \frac{a\sqrt{3}}{4},\qquad L_B = \frac{a\sqrt{2}}{4}. \tag{6}$$

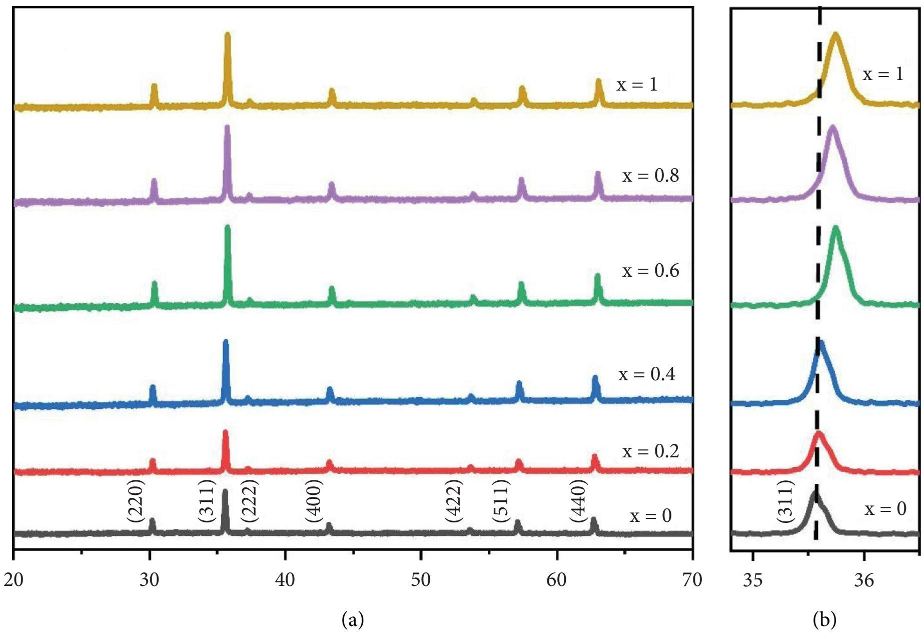

Figure 4: XRD pattern of all the compositions $Co_{1-x}Ni_xFe_2O_4$ (where $x = 0.0 \leq x \leq 1.0$) calcinated at 800°C along with the magnified view of (311) peaks.

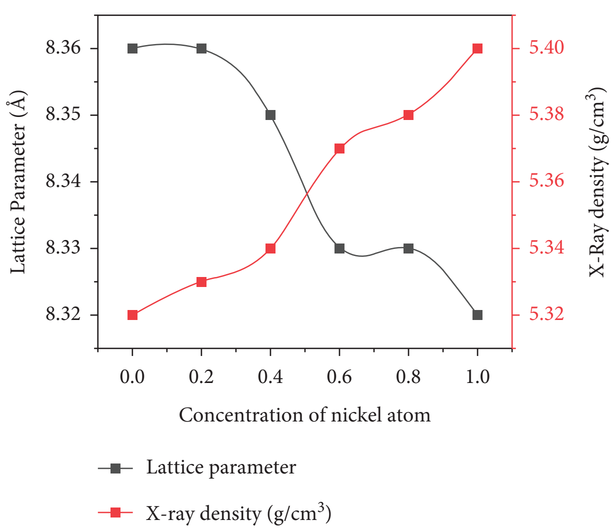

Figure 5: Variation of lattice parameter (a) and X-ray density (ρ_x) as functions of Ni^{2+} content.

Table 2 shows the computed values of the hopping length L_A and L_B of the various compositions. As the Ni^{2+}-substitution varies, the hopping length changes as well. The amount in the tetrahedral and octahedral sites at which Ni^{2+} substitution changes with increased Ni^{2+} concentration, has a great effect in changing the value of hopping length, which is connected to the fact that Ni^{2+} ion has lower ionic radii than Co^{2+} ion.

Specific surface area (S) was estimated by using the following relation:

$$S = \frac{6000}{D * \rho_x}, \quad (7)$$

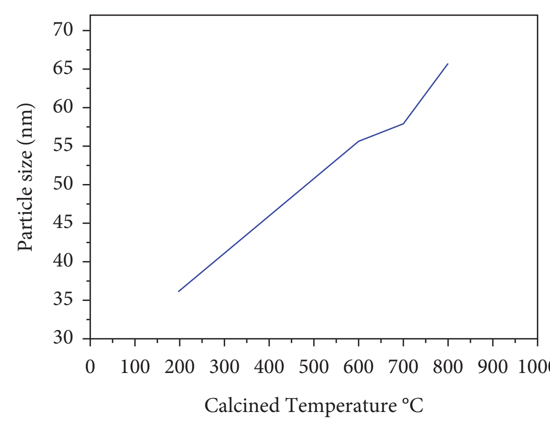

Figure 6: Variation of particle size (D) with calcination temperature.

where D is the crystallite size and ρ_x is the X-ray density [38].

The packing factor (P), another structural parameter that depends on crystallite size, was calculated using the following relation [39]:

$$P = \frac{D}{d_{(hkl)}}. \quad (8)$$

The calculated values of the packing factor for the $Co_{1-x}Ni_xFe_2O_4$ (where $x = 0.0 \leq x \leq 1.0$) nanoferrite particle samples were presented in Table 2. It was observed that with increasing Ni^{2+} concentration, the crystallite size decreases and a similar trend is observed for the packing factor values.

The structural refinement was carried out using the Rietveld refinement approach [40–42] with the fullprof program after the computation of structural parameters was carried out. Wyckoff positions for cobalt, nickel, and iron,

TABLE 2: Calculated values of various structural parameters for $Co_{1-x}Ni_xFe_2O_4$ (where $x = 0.0 \le x \le 1.0$) nanoferrites, for dominant peak (311) at $T = 800°C$.

Parameters	Composition (x)					
	0.0	0.2	0.4	0.6	0.8	1.0
Lattice parameter a (Å)	8.367	8.361	8.357	8.327	8.332	8.328
Crystallite size D (nm)	65.69	64.179	60.903	65.723	55.273	49.682
Unit cell volume $(Å)^3$	585.912	584.61	583.669	577.419	578.56	577.62
X-ray density ρ_x (g/cm^3)	5.321	5.332	5.339	5.396	5.384	5.392
Bulk density ρ_B (g/cm^3)	0.807	0.91	0.796	0.955	1.004	0.963
% porosity	84.817	82.925	85.087	82.302	81.35	82.126
The hopping length in A-site L_A (Å)	3.623	3.62	3.618	3.605	3.608	3.606
The hopping length in B-site L_B (Å)	2.958	2.956	2.954	2.944	2.946	2.944
Surface area (m^2/gm)	17.164	17.533	18.45	16.917	20.159	22.396
Packing factor	26.036	25.456	24.17	26.176	22	19.785

cations were taken at 8*a* (1/8, 1/8, 1/8), 16*d* (1/2, 1/2, 1/2), respectively, and 32*e* (*x*, *y*, *z*) for oxygen for the Fd-3m space group in cubic spinel ferrites [43]. Results of refinement for typical samples ($CoFe_2O_4$, $Co_{0.6}Ni_{0.4}Fe_2O_4$, and $NiFe_2O_4$) are shown in Figure 7. Based on the visual difference between observed-calculated intensities and the χ^2 parameter the goodness of fit was decided.

The refined values of the reliability parameters along with the goodness of fit factor (χ^2) index, lattice parameter, and volume of unit cells are listed in Table 3.

Due to the difference in the ionic radii of Ni^{2+} ions and Co^{2+} ions lattice constant of all the samples decreases with increasing Ni^{2+} content. Figure 8 illustrates the computational modeling structure of the typical sample $Co_{1-x}Ni_xFe_2O_4$ ($x = 0.4$) created with VESTA software, a program in which 2D and 3D structures of atoms and molecules of the crystal structure can be visualized and modeled. The crystal structure is represented by the ball and stick model, where oxygen is represented by small spheres and either cobalt and nickel or iron is represented by large spheres, and the polyhedral model, where octahedral sites and tetrahedral sites are presented within the crystal structure [44].

4.2. Vibrational Spectral Analysis. Typical room-temperature Fourier transform infrared (FTIR) spectra, for ($Co_{1-x}Ni_xFe_2O_4$(where $x = 0.0 \le x \le 1.0$) nanoferrite particle samples calcinated at 800°C recorded by using (Shimadzu, IRAffinity-1, Japan) by means of KBr pellets is depicted in Figure 9. The spectra obtained for the samples in the frequency range of 300–4000 cm^{-1}. All of the samples' functional groups have two separate absorption bands below 700 cm^{-1}, which support ferrite crystallization and also confirm the spinel structure of the samples. All the samples show an absorption band around 560–590 cm^{-1} and 390–400 cm^{-1} which are found to agree with the previously reported values [25, 27].

Wadron and Hafner have attributed that the higher absorption band (ν_1) around 560–590 cm^{-1} is appointed as the tetrahedral metal complex groups stretching vibration (Fe^{3+}-O^{2-}), which consists of bonding between A-site metal cation and oxygen anion. The lower absorption band (ν_2) around 390–400 cm^{-1} is attributed to the octahedral metal complex groups stretching vibration (Fe^{3+}-O^{2-}), which is regarded as bonding between B-site metal cation and oxygen anion [45]. Changes in metal-oxygen bond length (Fe^{3+}-O^{2-}) at both tetrahedral and octahedral coordination are attributed to the formation of two main absorption bands below 700 cm^{-1} [45]. The Debye temperature is the temperature at which the lattice exhibits the maximum vibration. For all the samples, the following equation is used to calculate the Debye temperature [45]:

$$\theta_D = \frac{hc\nu_{12}}{k_\beta}, \tag{9}$$

where c stands for the velocity of light ($3 * 10^8$m/s), k_β denotes Boltzmann's constant ($1.38 * 10^{-23}$J/K), h represents Plank's constant ($6.624 * 10^{-34}$J.s), and ν_{12} corresponds to the average wavenumber of absorption bands expressed as $\nu_{12} = (\nu_1 + \nu_2/2)$, ν_1 and ν_2 are the frequency of absorption bands related to A-site and B-site. With increasing calcination temperature, the Debye temperature increases, which corresponds to an increase in the normal vibration mode of the crystal. The calculated values of the absorption bands, average absorption bands, and Debye temperature are given in Table 4.

4.3. Field-Emission Scanning Electron Microscopy (FESEM). The cross-sectional morphology of the $Co_{1-x}Ni_xFe_2O_4$ (where $x = 0.0 \le x \le 1.0$) nanoparticles was analyzed by the field-emission scanning electron microscopy (FESEM) (Mira3-XMU, TESCAN, Japan). FESEM micrographs of the $CoFe_2O_4$, $Co_{0.6}Ni_{0.4}Fe_2O_4$, and $NiFe_2O_4$ nanoferrite particle samples calcinated at 800°C are shown in Figure 10.

The ferrites were investigated using FESEM to better understand their morphological microstructures. It illustrates that most of the nanoparticles have a nearly spherical shape. The nanoparticles have a nonuniform and inhomogeneous size distribution. The estimated average grain size diameter of spherical particles for $CoFe_2O_4$, $Co_{0.6}Ni_{0.4}Fe_2O_4$, and $NiFe_2O_4$ calcined at 800°C is found to be 139.4, 107.4, and 113.5 nm along with a standard deviation of 67.57, 56.28, and 61.97 nm, this decrease might be due to the lower ionic radii of nickel ions than cobalt ions.

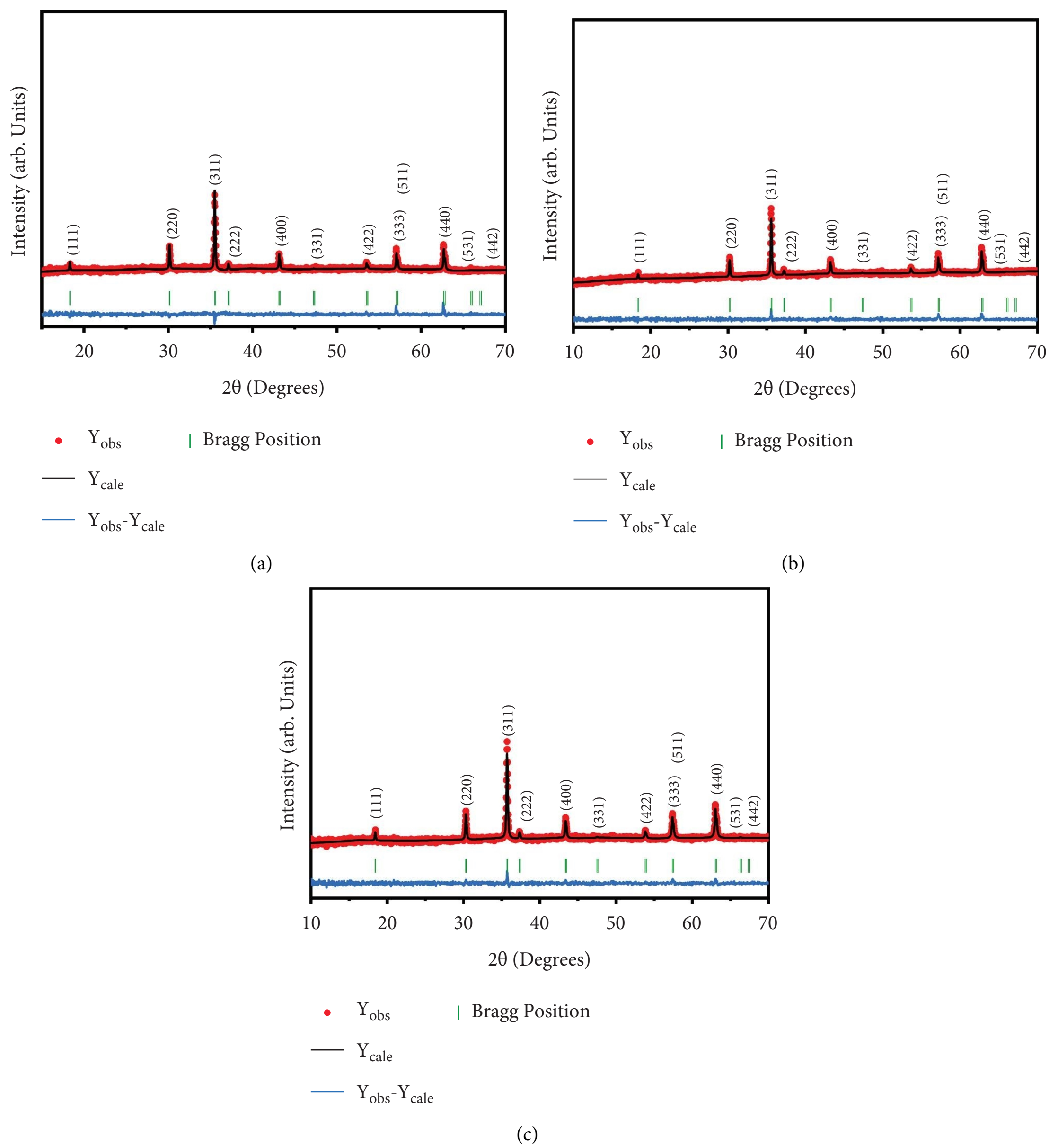

Figure 7: Rietveld refinement XRD plot for the typical (a) $CoFe_2O_4$, (b) $Co_{0.6}Ni_{0.4}Fe_2O_4$, and (c) $NiFe_2O_4$ samples. The measured data points (Y_{obs}.) are represented by red solid circles. The black solid lines correspond to calculated patterns (Y_{calc}). The green vertical lines are the Bragg positions. The difference between observed and calculated ($Y_{obs}- Y_{calc}$) plots is also shown as lines in blue color at the bottom of each pattern.

Table 3: Parameters obtained from Rietveld refinement for $Co_{1-x}Ni_xFe_2O_4$ (where $x = 0.0 \leq x \leq 1.0$) samples.

Parameters	Composition (x)					
	0.0	0.2	0.4	0.6	0.8	1.0
Profile factor R_p (%)	47.4	53.3	49	96.8	29.6	42.2
Weighted residual factor R_{wp} (%)	25.9	24.4	22.2	23.9	18	18.4
Expected residual factor R_{exp} (%)	19.73	22.07	19.27	17.61	13.17	17.46
Bragg R factor R_B (%)	14.2	21.7	15.7	39	3.9	5.16
R_F (%)	15	20.4	12.6	39.9	4.02	5.73
Goodness of fit χ^2 (%)	1.72	1.22	1.33	1.84	1.87	1.11
Lattice constant a (Å)	8.379	8.374	8.366	8.356	8.347	8.337
Unit cell volume V (Å^3)	588.36	586.47	585.7	583.63	581.59	579.57

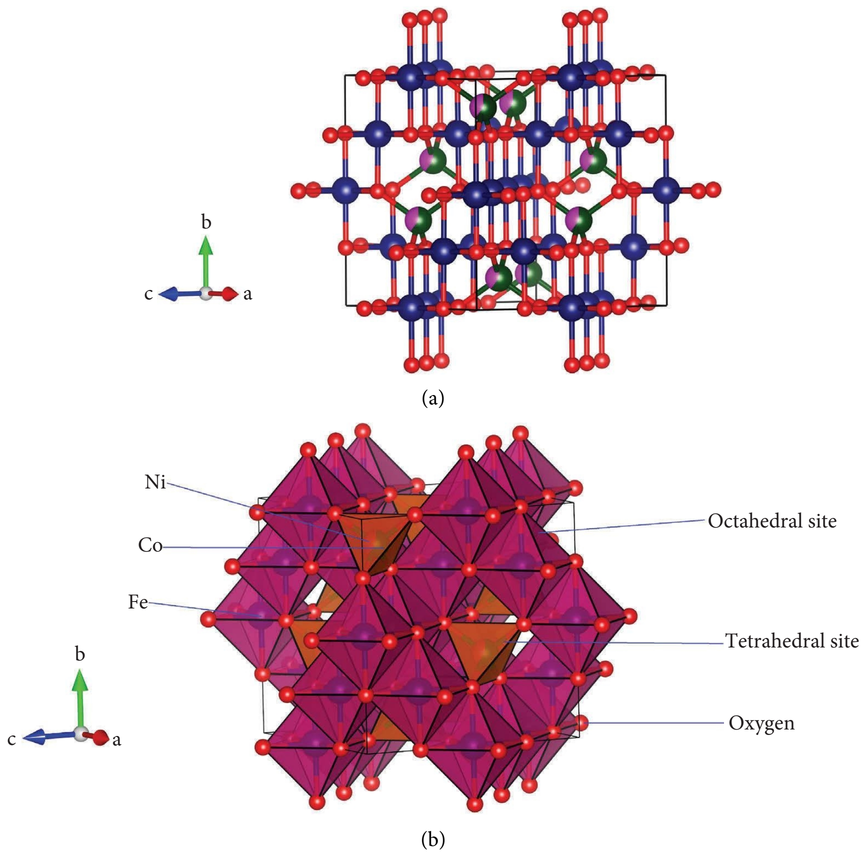

FIGURE 8: Typical polyhedral model crystal structure of $Co_{0.6}Ni_{0.4}Fe_2O_4$: (a) ball and stick model and (b) polyhedral model.

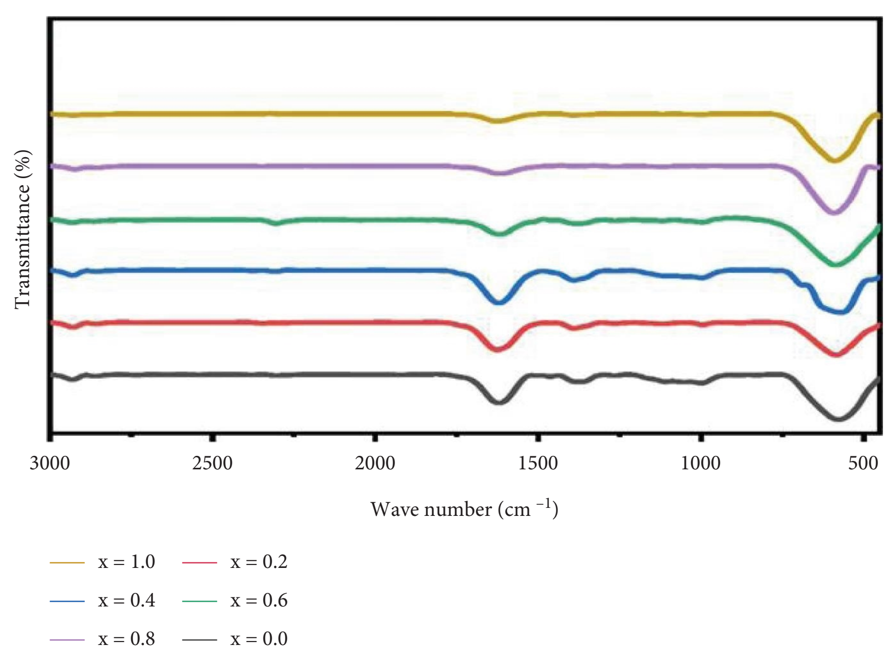

FIGURE 9: FTIR spectra of the prepared $Co_{1-x}Ni_xFe_2O_4$ (where $x = 0.0 \le x \le 1.0$) nanoferrite particle samples calcinated at 800°C.

The agglomeration is an indication of the prepared sample's high reactivity during heat treatment, and it could possibly be due to magnetostatics interaction between the nanoparticles as the magnetic nanoparticles attract each other by Van der Waals forces and magnetic dipolar interactions [46]. The formation of agglomerated grain structure is a characteristic feature of the sol-gel autocombustion process.

Table 4: FTIR absorption data for $Co_{1-x}Ni_xFe_2O_4$ (where $x = 0.0 \le x \le 1.0$) calcinated at 800°C.

Parameters	Composition (x)					
	0.0	0.2	0.4	0.6	0.8	1.0
ν_1 (cm^{-1})	573.56	588.14	573.32	583.39	588.14	588.14
ν_2 (cm^{-1})	398.28	401.38	396.64	391.89	401.38	401.38
ν_{12} (cm^{-1})	485.92	494.76	484.98	487.64	494.76	494.76
θ_D (K)	69.972	71.245	69.837	70.220	71.245	71.245

4.4. Energy-Dispersive Spectrum (EDS). The attached energy-dispersive spectrum (EDS) model Aztec (Oxford instrument PLC, UK) was used to investigate the qualitative chemical composition of the samples which was carried out to accurately indicate and confirm the existence of Ni, Co, Fe, and O present in the compositions. The energy dispersive spectrum shows that nearly the same stoichiometric amount of the elements is present in the chemical composition without any major impurity. Typical EDS patterns of samples calcined at 800°C are depicted in Figure 11. Table 5 summarizes the weight and atomic percentages of individual $Co_{1-x}Ni_xFe_2O_4$ (where $x = 0.0 \le x \le 1.0$) nanoferrite particle samples calcinated at 800°C. The theoretical weight percentages from the stoichiometric formula compared to the experimentally established percentages are listed in Table 5.

4.5. Transmission Electron Microscopy (TEM). Transmission electron microscopy (TEM) measurements were recorded at operating voltages of 200 kV. Typical high-resolution TEM micrographs for the $CoFe_2O_4$ and $Co_{0.6}Ni_{0.4}Fe_2O_4$ nanoparticle samples calcined at 800°C are depicted in Figure 12. The majority of particles in the TEM images show to be spherical in shape and have a polycrystalline nature. Because of the sample's strong magnetic nature, by interfacial forces, a large number of small particles are held together and compose these bigger spherical (agglomerate) shape particles. The estimated average particle size is 82.51 and 52.31 nm along with a standard deviation of 41.81 and 28.21 nm united together to form aggregates due to their small sizes, due to the interaction between magnetic particles some agglomeration occurs during the calcination at 800°C. Substitution of Ni^{2+} ions into cobalt ferrite causes a decrease in particle size. The particle size distribution histograms are shown as an inset in Figure 12.

4.6. Dielectric Properties. The LCR meter (Keysight E4980A/AL Precision LCR meter) device was used to study the dielectric behavior at different frequencies (20 Hz–2 MHz) regions. The complex permittivity of all the $Co_{1-x}Ni_xFe_2O_4$ (where $x = 0.0 \le x \le 1.0$) nanoferrite particle samples calcinated at 800°C was calculated. For that purpose, the dielectric constants' (ε') values (also known as the real permittivity) of all samples are measured using the following formula by using their known capacitance at room temperature (Figure 13(a)):

$$\varepsilon' = \frac{Cd}{A\varepsilon_o}, \tag{10}$$

where C corresponds to the capacitance of the sample, ε_o is the permittivity of the vacuum, A represents the area of the sample, and d is the thickness of the sample.

It exhibits dielectric dispersion at lower frequencies and achieves a stabilized relaxing value at higher frequencies, based on the Maxwell–Wagner model of interfacial polarization and exactly corresponding to Koop's phenomenological theory of dispersion [47]. Conducting grains and insulating grain boundaries are the two layers of the dielectric structure according to this theory.

The average grain size of specimens is related to the dielectric constant of the same composition. As a result, at lower frequencies, the decrease is rapid. Because the electron exchange between ferric and ions ferrous is not followed by the alternating field at higher frequencies, the rate of decrease in dielectric constant with respect to frequency slows down [48]. An overall increase is noticed in the value of the dielectric constant with respect to the substitution of Ni^{2+} in place of cobalt except for a slight decrease for compositions ($x = 0.2, 0.4$). The maximum values are possessed by ($x = 1.0$) compositions.

Also, for the calculation of dielectric loss (ε'') along with AC conductivity (σ_{AC}) of the samples, the dielectric constant (ε') and the dissipation factor ($\tan\delta$) were used. The relations used for these measurements are as follows [49]:

$$\begin{aligned} \varepsilon'' &= \tan\delta \times \varepsilon', \\ \sigma_{AC} &= \omega\varepsilon_o\varepsilon' \tan\delta, \end{aligned} \tag{11}$$

where ω represents the angular frequency. The variation of the dielectric constant with respect to frequency is similar to that of the dielectric loss as shown in Figure 13(b). At higher frequencies, the decrease in space charge polarization causes a decrease in dielectric loss [50].

The value of AC conductivity increases linearly with frequency for all the samples, which is the expected characteristic of ferrites Figure 13(c). It can be explained by Verwey's hopping mechanism [51], which states that electrical conductivity in ferrites is mostly caused by electron hopping between ions of the same element in more than one valence state [52]. Conductive grains become increasingly active at higher frequencies of the applied field, also the conductivity increases due to an increase in the hopping frequency [53]. The AC conductivity increases when doping is increased from ($x = 0.0$ to $x = 1.0$) since a high proportion of Ni^{2+} ions choose A-sites and contribute to hopping transport. Because the amount of charge carriers, i.e., electrons, has increased, the conductivity has increased as well.

4.7. Magnetic Properties Using Vibrating Sample Magnetometer (VSM). The magnetic properties were investigated at room temperature using a vibrating sample magnetometer (LBKFB model Meghnatis Daghigh Kavir Company) in the applied field range of −15 to +15 kOe. Figure 14 shows a typical magnetic hysteresis loop obtained at room temperature for nanocrystalline $Co_{1-x}Ni_xFe_2O_4$ (where $x = 0.0 \le x \le 1.0$) nanoferrite particle samples calcinated at

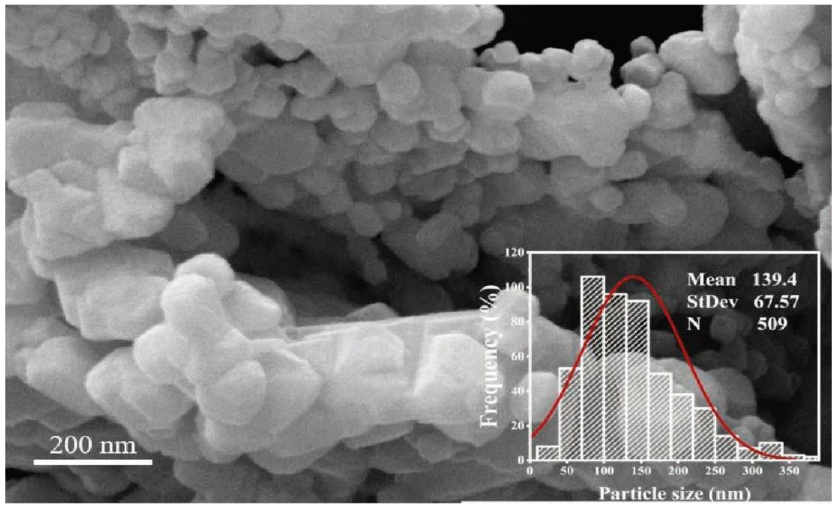

(a)

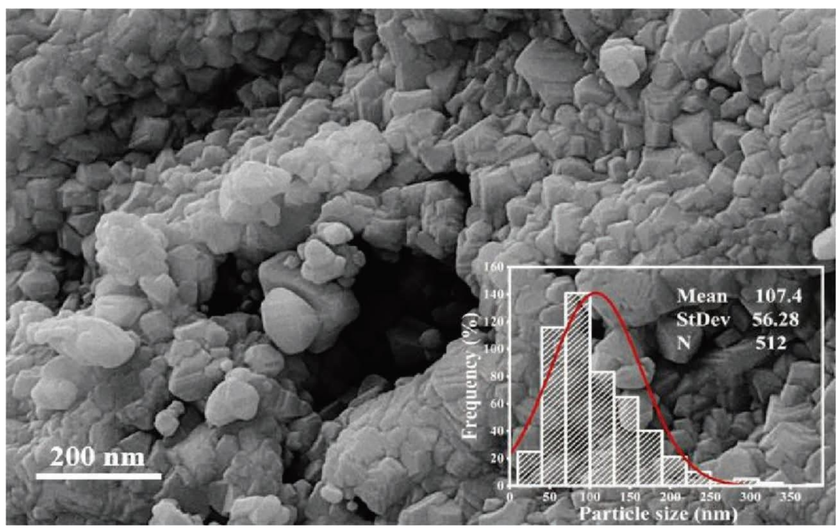

(b)

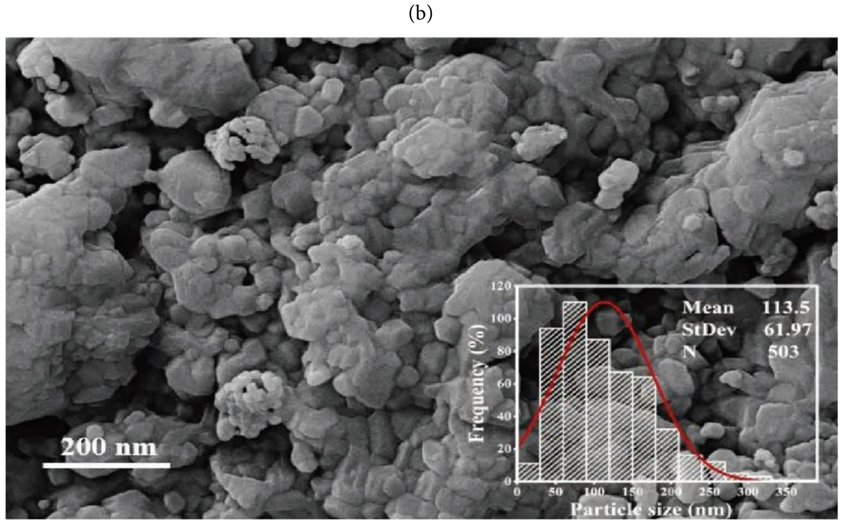

(c)

FIGURE 10: FESEM micrograph of the (a) $CoFe_2O_4$, (b) $Co_{0.6}Ni_{0.4}Fe_2O_4$, and (c) $NiFe_2O_4$ nanoferrite particle samples calcinated at 800°C, the (Inset) corresponding histogram.

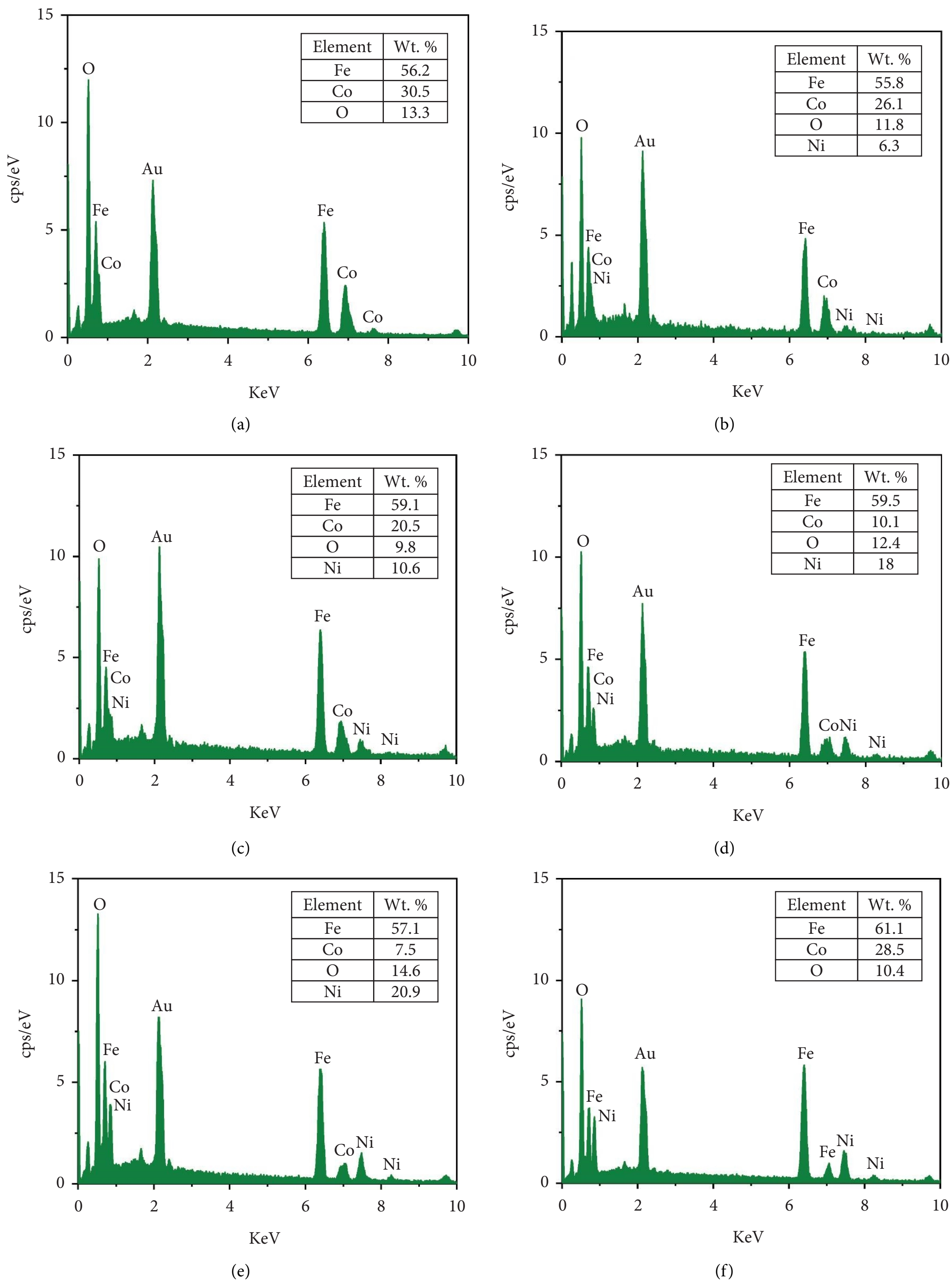

Figure 11: Elemental weight composition of nickel-substituted cobalt ferrite: (a) $x = 0.0$, (b) $x = 0.2$, (c) $x = 0.4$, (d) $x = 0.6$, (e) $x = 0.8$, and (f) $x = 1.0$.

800°C, and magnified magnetization curves are shown as an inset in the figure under low applied magnetic field. All of the samples had ferrimagnetic properties with S-shaped hysteresis loops.

The decrease in saturation magnetization with decreasing cobalt concentration can be explained by the fact that due to their relatively strong orbital contribution to magnetic moment Co^{2+} ions are known to have considerable

Table 5: Experimental values obtained from the spectrum of energy dispersive X-ray analysis for $Co_{1-x}Ni_xFe_2O_4$ (where $x = 0.0 \le x \le 1.0$) calcinated at 800°C.

Composition	Elements	Wt. (%)		% atomic
		EDS	Theoretical	
$x = 0.0$	Fe	56.2	47.6	28.6
	O	13.3	27.28	57.1
	Co	30.5	25.12	14.3
	Ni			
$x = 0.2$	Fe	55.8	47.61	28.6
	O	11.8	27.28	57.1
	Co	26.1	20.1	11.4
	Ni	6.3	5.01	2.9
$x = 0.4$	Fe	59.1	47.62	28.6
	O	9.8	27.29	57.1
	Co	20.5	15.08	8.57
	Ni	10.6	10.01	5.73
$x = 0.6$	Fe	59.5	47.63	28.6
	O	12.4	27.29	57.1
	Co	10.1	10.06	5.71
	Ni	18	15.02	8.59
$x = 0.8$	Fe	57.1	47.64	28.6
	O	14.6	27.3	57.14
	Co	7.5	5.03	2.86
	Ni	20.9	20.03	11.4
$x = 1.0$	Fe	61.1	47.65	28.6
	O	10.4	27.3	57.1
	Co			
	Ni	28.5	25.05	14.3

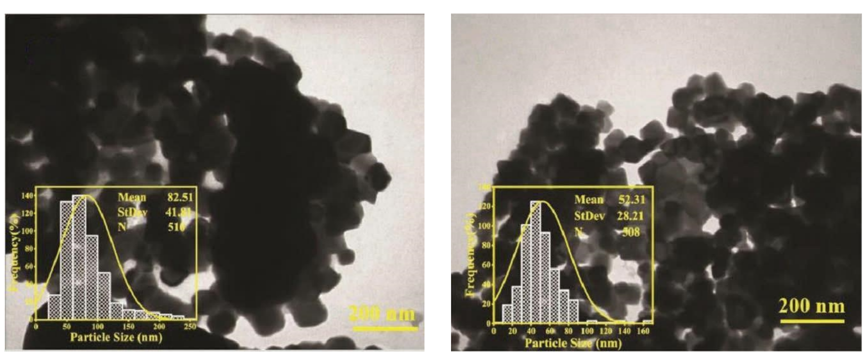

(a) (b)

Figure 12: TEM micrographs and (inset) particle distribution histogram of the (a) $CoFe_2O_4$ and (b) $Co_{0.6}Ni_{0.4}Fe_2O_4$ ferrite nanoparticle samples calcinated at 800°C.

induced anisotropy [54]. Increasing Ni^{2+} concentration causes a decrease in coercivity, and this may be due to the decrease in the anisotropy field, which in turn decreases the domain wall energy [55, 56].

In the present study, the saturation magnetization values are very high, and close to that of the bulk cobalt ferrite indicating that the sol-gel autocombustion technique is a good synthesis method. An increase in particle size as the calcined temperature increases may also cause the saturation magnetization to increase. However, $CoFe_2O_4$ has higher saturation magnetization than $NiFe_2O_4$ due to the high ionic magnetic moment of Co than Ni. Similar high saturation magnetization values have been reported in the literature by several authors [57–60]. The magnetization increases with an increase in grain size as the surface-to-volume ratio decreases [61, 62]. The magnetic studies revealed that another reason for a high value of saturation magnetization is due to canting of spins occurrence as explained by the Yafet–Kittel model. The smaller canting angle of magnetic ions shows the increase in the overlap of the wave functions between the two nearest neighboring magnetic ions and also superexchange interactions between the magnetic ions and oxygen anions lead to a higher saturation magnetization [63].

For the spinel ferrites, the cations in tetrahedral (A-site) and octahedral (B-site) have opposite aligned magnetic

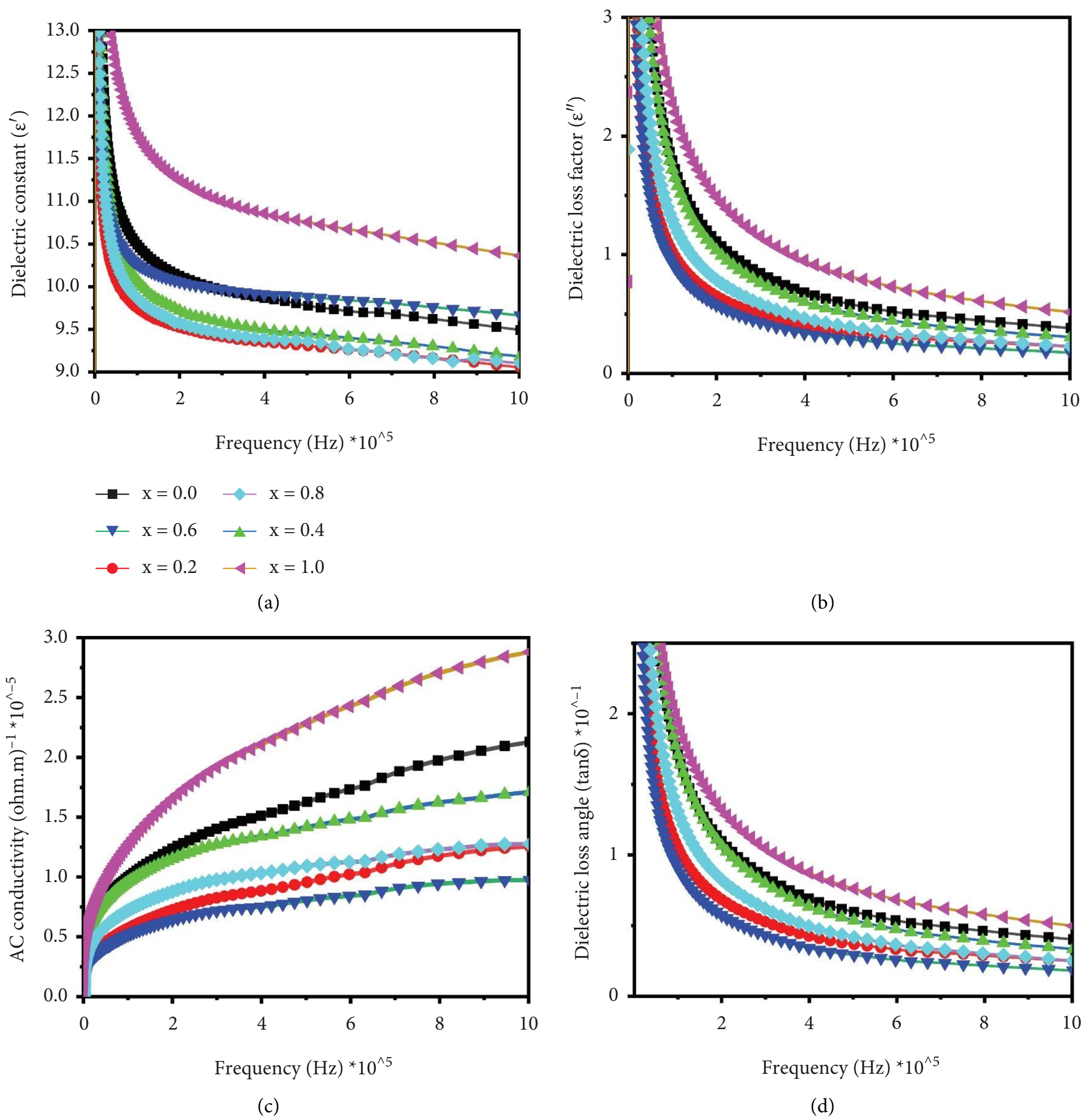

Figure 13: Dielectric parameters of all the prepared $Co_{1-x}Ni_xFe_2O_4$ (where $x = 0.0 \leq x \leq 1.0$) nanoparticle samples calcinated at 800°C.

moments, where the theoretical magnetic moment values n_B^{th} of $Co_{1-x}Ni_xFe_2O_4$ ferrite nanoparticles were calculated using the proposed cation distribution and the ionic magnetic moment [64].

$$n_B^{th} = M_B - M_A, \tag{12}$$

where M_B and M_A are the Bohr magneton on the A-site and B-site, respectively.

The experimental value of magnetic moment (n_B^e in units of Bohr magneton) was computed using the following relation [65]:

$$n_B^e = \frac{M_{\text{spinelferrite}} \times M_s}{5585}, \tag{13}$$

where $M_{\text{Spinelferrite}}$ is the molecular weight of the synthesized ferrite in g/mol, 5585 is the magnetic factor, and M_s is saturation magnetization in emu/g.

Because the experimental values of the magnetic moment are smaller than the theoretical magnetic moment which means that Neel's two-sub-lattice collinear model is not suitable for the obtained samples and the magnetic order is not governed by the Neel-type magnetic order. This difference between the theoretical and experimental magnetic moment showed that we need to invoke Yafet–Kittel three sublattice model. This suggests that the magnetic order in all the nickel-substituted cobalt ferrite samples shows a Y-K type of magnetic ordering.

According to the Neel model when the canting angle is zero means that the sample shows a Neel-type of magnetic ordering indicating that magnetization can be explained on the basis of the Neels two sublattice theory. While, according to the Y-K model, the B lattice can be divided into two sublattices, B_1 and B_2, each having magnetic moments equal in magnitude and each oppositely canted at the same angle

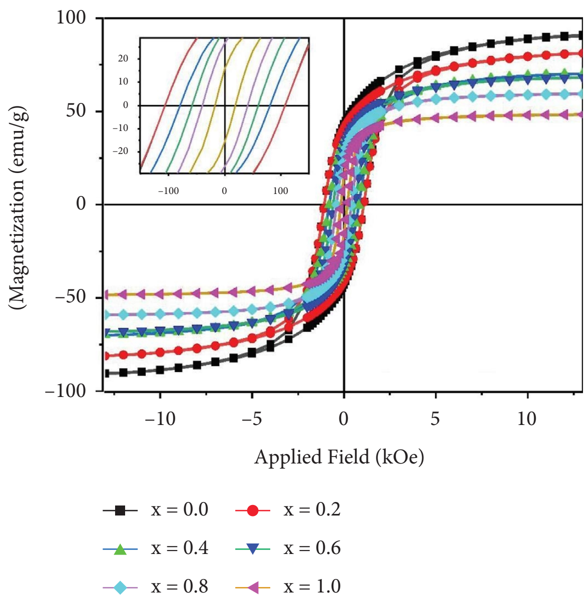

FIGURE 14: Magnetic hysteresis loops for $Co_{1-x}Ni_xFe_2O_4$ (where $x = 0.0 \leq x \leq 1.0$) nanoferrite particle samples calcinated at 800°C; inset showing magnified hysteresis loops under low magnetic field.

α_{Y-K} (being the angle between the moments on the B_1 and B_2 sites), relative to the net magnetization at 0 K. In this way, the two sublattices B_1 and B_2 have the triangular type spin arrangements which become more significant with changing concentration. The resultant moment of the B sublattice is still collinear but antiparallel to that of the A sublattice. The existence of canted spin in the ferrimagnetic structure and the behavior of the magnetic moment with increasing Ni^{2+} concentration can be observed by determining the Y-K angle. The values of the spin canting angle (Yafet–Kittel angle) between the moments in B site from the experimental magnetic moment is calculated by using the formula as follows [66, 67]:

$$\alpha_{Y-K} = \cos^{-1}\left(\frac{n_B^e + M_A}{M_B}\right). \tag{14}$$

Moreover, there is a significant triangular (or canted) noncollinear type spin arrangement in B-site, since for all the samples the calculated values of Y-K angles are nonzero, which strengthens the B-B interaction and in turn, reduces the A-B interaction. The system can be explained according to the Yafet and Kittel three sublattice model. The increase in spin canting angles for the samples with an increase in Ni^{2+} content suggests the increased favor for triangular spin arrangements on B sites resulting in the decrease in the A-B exchange interaction and thus enhancing the B-B interaction.

From experimental results, it is observed that the values of M_s and hence n_B goes on decreasing as the concentration of Ni^{2+} is increased. The decrease in M_s and hence n_B for all the samples is caused by nonzero Y-K angles.

In the present study, the calculated squareness ratio for compositions $x = 0.0$, 0.2, 0.4, 0.6 (high H_c) has been found to be nearly 0.5, indicating that these samples have a virtually single domain structure and correspond to uniaxial anisotropy, while the other compositions $x = 0.8$, and 1.0 (lower H_c) possess a ratio of 0.43 and 0.32 respectively, attributed to that these ferrites have a multidomain structure, also according to the Stoner–Wohlfarth model squareness ratio of an assembly of noninteracting 3D random particles is 0.5, it can be concluded that all the samples in this study have uniaxial anisotropy because the squareness values are nearly equal or lower than 0.5 [68].

The calculated values obtained from Figure 14 of saturation magnetization M_s, coercivity H_c, remanent magnetization M_r, squareness ratio M_r/M_s, experimental n_B^e and theoretical n_B^{th} magnetic moment, and Y-K angles (α_{Y-K}) with respect of Ni^{2+} concentration for all the samples calcined at 800°C are listed in Table 6.

For ($NiFe_2O_4$) composition the values of all the magnetic parameters are much lower than other compositions. A noticeable decrease in M_r from 42.89 emu/g to 15.49 emu/g is found with an increase in x from (0.0 to 1.0).

4.8. Vector Network Analyzer (VNA). The blocking of incident electromagnetic radiation is known as electromagnetic interference (EMI). Possible EMI shielding based on $Co_{1-x}Ni_xFe_2O_4$/PVA nanocomposites has been proposed and illustrated in Figure 15. When EM radiation incident on the shielding surface because of multiple/internal reflections through the Ni^{2+} substituted cobalt ferrite/PVA interfaces that exist in the shielding nanocomposite film, from the outer side of the nanocomposite film some EM radiation is reflected, a small portion is transmitted from the film, and within the nanocomposite, the remaining EM radiation is absorbed. Many different ways can be used to measure EMI shielding such as impedance parameters [69], electrical and magnetical parameters [70], and VNA [71, 72].

A novel and promising application of the electromagnetic $Co_{1-x}Ni_xFe_2O_4$/PVA nanocomposites is their ability to shield electromagnetic radiation. The mechanisms of energy loss in magnetic materials are due to dielectric and magnetic properties, which depend on the imaginary part of the complex permittivity and complex permeability. The EM shielding performances of the $Co_{1-x}Ni_xFe_2O_4$/PVA nanocomposites films were analyzed by vector network analyzer an Agilent N5230 A (Keysight Technologies, Inc. USA) in the X-band (8.2–12.4) GHz, by calculating the scattering parameters (S-parameters) for a rectangular strip with dimensions (10.16 ∗ 22.86 mm) of nanocomposite film samples.

EMI shielding was calculated from scattering S-parameters and then complex values of permittivity and permeability were calculated using the Nicholson–Ross method to investigate the underlying shielding mechanisms of $Co_{1-x}Ni_xFe_2O_4$/PVA nanocomposites films and understand the shielding mechanism. The method used to measure reflection loss (RL) using complex electromagnetic parameters obtained experimentally is a short-circuit approach, in which RL values are simulated [73]. The electromagnetic parameters, that is, complex dielectric permittivity ($\varepsilon_r = \varepsilon_r' - j\varepsilon_r''$) and magnetic permeability

Table 6: Magnetic properties of different compositions of $Co_{1-x}Ni_xFe_2O_4$ (where $x = 0.0 \le x \le 1.0$) nanoferrite particle samples calcinated at 800°C.

Parameters	Compositions (x)					
	0.0	0.2	0.4	0.6	0.8	1.0
M_s (emu/g)	91.01	81.69	70.69	68.26	59.55	48.38
H_c (Oe)	1072	1077	807	598	407	183
M_r (emu/g)	42.89	42.89	33.78	32.007	26.18	15.49
n_B^e	3.823	3.430	2.968	2.865	2.499	2.030
M_r / M_s	0.471	0.525	0.477	0.468	0.439	0.320
n_B^{th}	3.72	3.92	3.92	3.85	3.92	3.98
α_{Y-K}	14.53	19.69	27.77	28.49	34.53	40.88

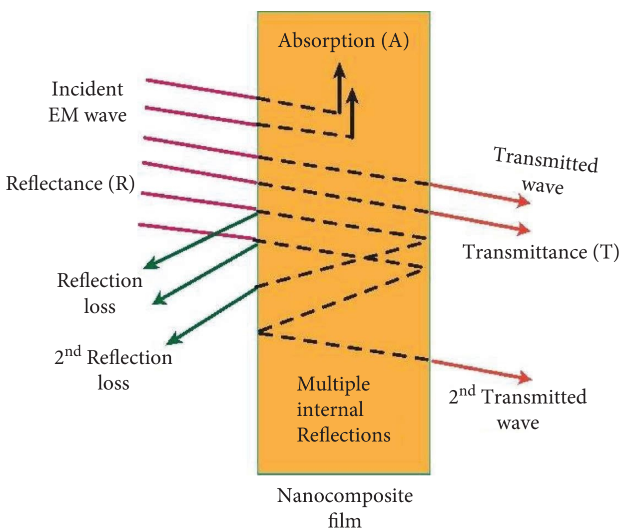

Figure 15: Schematic illustration of EMI shielding mechanism based on $Co_{1-x}Ni_xFe_2O_4$/PVA nanocomposites.

($\mu_r = \mu_r' - j\mu_r''$) parameters over the frequency range of (8.2–12.4) GHz are widely utilized and displayed in the Figures 16(a)–16(d) [74].

The PF2 sample gets the best positive values of permittivity of the real part (ε_r') and imaginary part (ε_r'') than another sample, i.e., with an increase in frequency an increase or little decreasing trend is observed. This is owing to the fact that the existence of bound charges (dipoles) contributes to the orientation polarization [75].

The values of complex magnetic permeability of the real part (μ_r') and imaginary part (μ_r'') are also in the positive range for all the samples at the frequency range (8.2–12.4) GHz. The permittivity and permeability analysis for microwave absorption, in addition to EMI shielding applications, revealed that the microwave absorption of PF2 composite is primarily attributed to dielectric and magnetic wave attenuation mechanisms acting together, which are essential for improving EM wave absorption applications [76]. As well as because of overlapping attenuation aggregate from ferrite and PVA that is causing the spurious values of the magnetic permeability.

When EM waves pass from a material, SE is expressed as the logarithmic ratio of incident P_i and transmitted P_o power of EM wave, mathematically expressed as in the following [77]:

$$\text{SE total (dB)} = 10\log_{10}\left(\frac{P_i}{P_o}\right). \quad (15)$$

The performance of shielding material to attenuate EMI can be expressed by the EMI shielding effectiveness and calculated in decibels (dB) units.

As the incident EM wave falls on the material, three basic interaction phenomena occur; transmittance (T), reflectance (R), and absorbance (A) [78]. The transmission coefficient and reflection coefficient are related to S-parameters as follows:

$$T = |S_{21}|^2 = |S_{12}|^2,$$
$$R = |S_{22}|^2 = |S_{11}|^2. \quad (16)$$

The scattering parameters represent S_{11} as the coefficient of forwarding reflection and S_{12} as the coefficient of reverse transmittance. The power of transmission and reflection characterizes the scattering parameter. In turn, from the above equations, the absorption coefficient is measured which is mathematically expressed as follows:

$$A = 1 - R - T. \quad (17)$$

The samples were bombarded by electromagnetic waves from both sides and scattering parameters were obtained from VNA and shielding effectiveness through absorbance (SE_A), shielding effectiveness through reflection (SE_R), and total shielding effectiveness (SE_T) were calculated using the following equations:

$$SE_A = -10 * \log_{10}\left(\frac{T}{1-R}\right),$$
$$SE_R\,(\text{dB}) = -10 * \log_{10}(1-R), \quad (18)$$
$$SE_T = SE_A + SE_R.$$

According to Schelkunoff's hypothesis, a material's total shielding effectiveness (SE_T) is determined by its electrical conductivity and is proportional to its reflection, absorption, and multiple reflections.

When the absorption loss is ≥10 dB, multiple/internal reflection is neglected for total SE. Because of absorption, while moving from one boundary to another the magnitude of EM waves is neglected at high frequencies. Materials with a high ability of absorption and high thickness can neglect safely multiple/internal reflections. As a result, only absorption loss (SE_A) and reflection loss (SE_R) contribute to SE_T [79]. The total EMI SE (measured directly from S-parameters) can be obtained as follows:

$$\text{EMI SE} = 10 * \log_{10}\frac{1}{|S_{12}|^2} = 10 * \log_{10}\frac{1}{|S_{21}|^2}. \quad (19)$$

Figure 17 shows the EMI shielding effectiveness values of prepared nanocomposite PF1, PF2, and PF3 samples in the frequency range X-band (8.2–12.4) GHz. The obtained result of EMI SE of PF2 is 27 dB. This result can be enhanced for the composites with higher magnetic permeability, electrical conductivity, and larger thicknesses [56]. Pubby et al. [28]

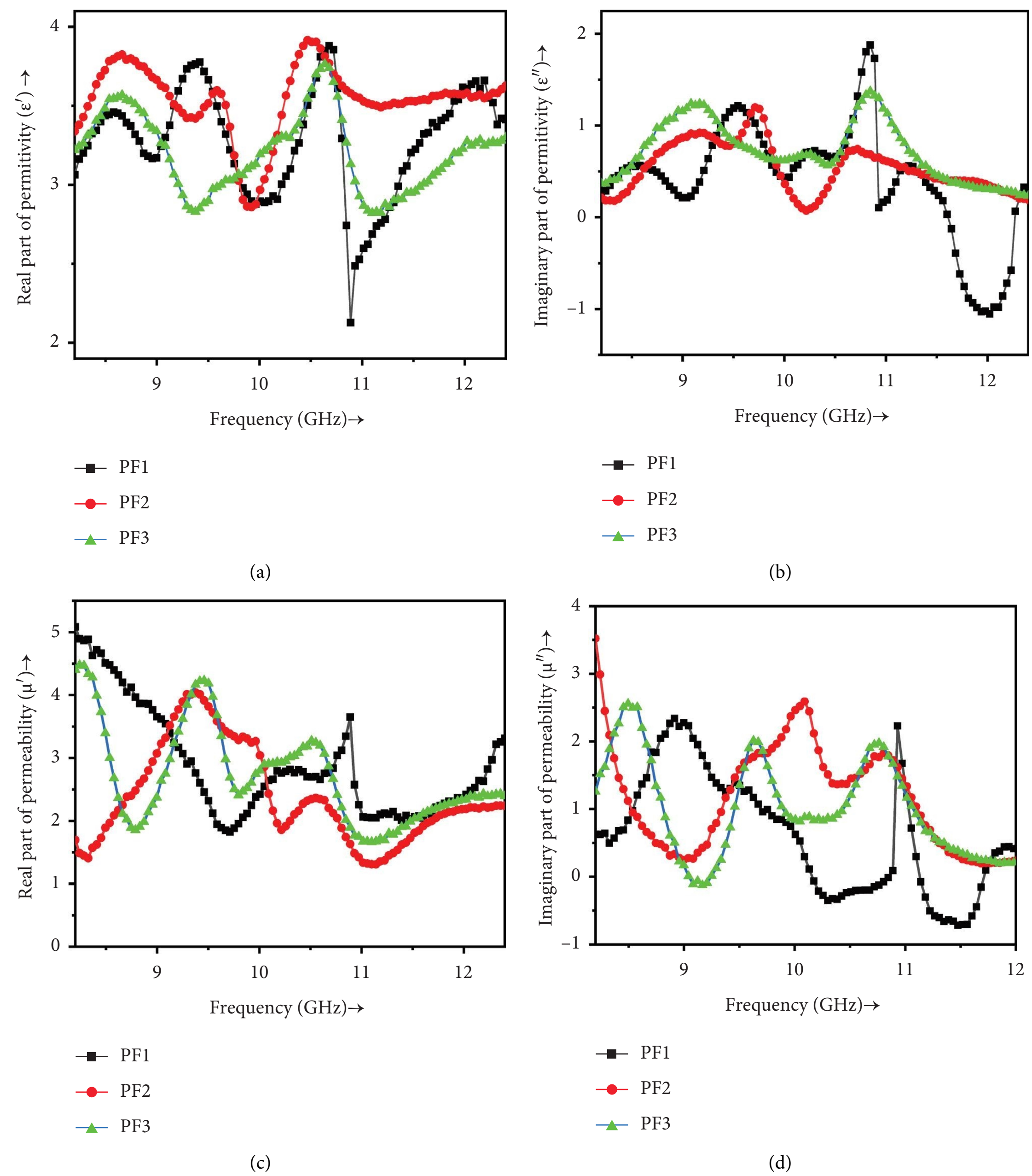

Figure 16: Complex dielectric permittivity (a) real (ε_r') and (b) imaginary (ε_r'') and complex magnetic permeability and (c) real (μ_r') and (d) imaginary (μ_r'') of PF1, PF2, and PF3 samples.

also reported a significant enhancement and increase in absorption shielding effectiveness parameters with the addition of cobalt in nickel ferrites, so they concluded that the mixed nickel-cobalt ferrite has potential for usage in microwave shielding applications.

The oscillatory behavior of absorption in the Ni^{2+} substituted cobalt nanoferrites samples are due to the hopping of electrons, diverse relaxation frequencies of various dipoles formed in the ferrite structure, and the relaxation due to interfacial polarization.

The Ni^{2+} substituted cobalt nanoferrites act as an absorbing material and show improved EMI shielding values due to their dielectric and magnetic losses in the microwave frequency band. The dielectric properties perfectly matched the magnetic properties. The magnetic loss of these magnetic materials results from their spin relaxation in the high-frequency alternating electromagnetic fields, ferrimagnetism's, and the resonance absorption of moving magnetic domains wall.

The advantage of using polymer nanocomposite is that a large number of nanoferrite particles can accommodate in small film thickness because of the small filler particle size, resulting in more EMR attenuation due to a large number of interfaces. All communication devices operate in the microwave range and emit electromagnetic radiation into the environment which can be shielded using the EMI shielding

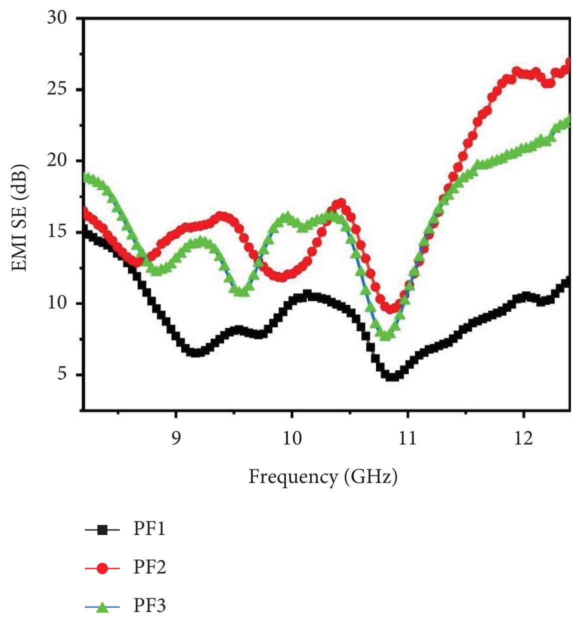

Figure 17: EMI SE (dB) of PF1, PF2, and PF3.

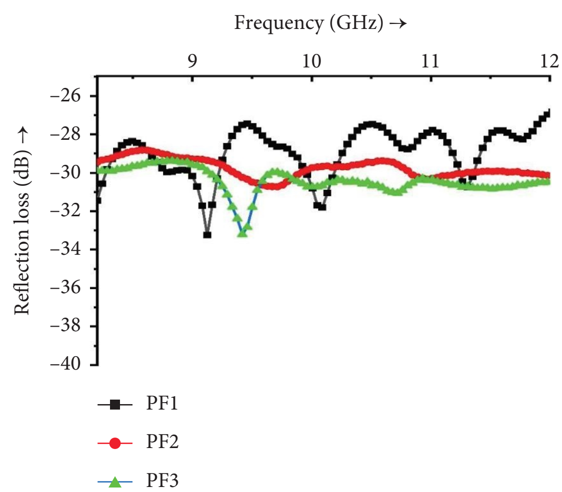

Figure 18: Absorption characteristics of the prepared PF1, PF2, and PF3 at X-band (8.2–12.4) GHz.

approach. The theory of EMI is based on essential mechanisms such as reflection loss and absorption loss. The transmission line theory method is used to calculate the frequency dependence of reflection loss (RL) at a thickness (d) based on data of complex dielectric permittivity and complex magnetic permeability, which characterizes the electromagnetic wave absorption properties [80].

$$Z_{\text{in}} = \sqrt{\frac{\mu_r}{\varepsilon_r}} \tan h \left(\frac{i2\pi f d \sqrt{\mu_r \varepsilon_r}}{c} \right),$$
$$R_L = 20 \log \left| \frac{Z_{\text{in}} - 1}{Z_{\text{in}} + 1} \right| (\text{dB}), \tag{20}$$

Table 7: Comparison of EMI shielding properties obtained in the present study with that of the various ferrites reported in the literature.

Ferrites	Synthesis route	Composition	Reflection loss (dB)	Frequency range (GHz)	Year	Ref.
$CoFe_2O_4$	Coprecipitation	$CoFe_2O_4$/paraffin wax	−48	0.1–20	2018	[81]
$NiFe_2O_4$	Coprecipitation	$NiFe_2O_4$/PANI	−35	0.1–20	2020	[82]
$Ni_{0.6}Zn_{0.4}(CoZr)_x Fe_{2\text{-}2x}O_4$	Sol-gel citrate	$Ni_{0.6}Zn_{0.4}(CoZr)_{0.05}Fe_{1.9}O_4$/PVA	−20.92	8.2–12.4	2020	[83]
		$Ni_{0.6}Zn_{0.4}(CoZr)_{0.1}Fe_{1.8}O_4$/PVA	—			
		$Ni_{0.6}Zn_{0.4}(CoZr)_{0.15}Fe_{1.7}O_4$/PVA	−36.78			
		$Ni_{0.6}Zn_{0.4}(CoZr)_{0.2}Fe_{1.6}O_4$/PVA	−44.92			
		$Ni_{0.6}Zn_{0.4}(CoZr)_{0.25}Fe_{1.5}O_4$/PVA	−40.43			
$CoFe_2O_4$	—	$CoFe_2O_4$/PANI-50	−34.4	2–20	2020	[84]
		$CoFe_2O_4$/PANI-40	−43.1			
		$CoFe_2O_4$/PANI-30	−38.9			
		$CoFe_2O_4$/PANI-20	−36.9			
		$CoFe_2O_4$/PANI-10	−11.7			
$Co_{0.5}Zn_{0.5}Fe_2O_4$	High energy ball milling followed by sintering	$Co_{0.5}Zn_{0.5}Fe_2O_4$/epoxy resin	−24.5	8–12	2018	[85]
$CoFe_2O_4$	Sol-gel autocombustion	$CoFe_2O_4$/PANI-PTSA	−28.4	8.2–12.4	2018	[56]
Ni^{2+} substituted cobalt	Sol-gel autocombustion	Ni^{2+} substituted cobalt/PVA	−32.08	8.2–12.4		Present study result

where Z_{in} is the absorber's input impedance, f represents the frequency, d is the absorber thickness, and c is the velocity of light. Figure 18 characterizes the measured absorption spectra of PF1, PF2, and PF3. The maximum RL for the prepared nanocomposites in the X-band frequency range is (−32.08 dB) for the PF2 sample.

To rationalize the discussion, we compared our results with those reported in the literature, and the data are comprehensively presented in Table 7.

5. Conclusions

Nanostructured Ni^{2+} substituted cobalt spinel ferrite with a composition of $Co_{1-x}Ni_xFe_2O_4$ (where $x = 0.0 \leq x \leq 1.0$) and the corresponding composite film was synthesized successfully. The obtained result demonstrates that variation in calcination temperature could turn effectively the structural, dielectric, and magnetic properties of $Co_{1-x}Ni_xFe_2O_4$ (where $x = 0.0 \leq x \leq 1.0$) nanoferrite particles. From XRD, the crystallite size of the synthesized samples was calculated and is found to be in the nano-range between 49 and 65 nm. Due to the substitution of Ni^{2+} ions, a decrease in the lattice parameters values and a shift of the main peak (311) towards a higher angle occurs. With increasing Ni^{2+} content a decrease in the grain size is observed. The nanocomposite films were successfully prepared through the solution casting technique. Shielding effectiveness of −32.08 dB was observed in a broad X-band of frequency regions (8.2–12.4) GHz.

Data Availability

All data used to support the findings of this study are included within the article.

Conflicts of Interest

The authors declare that they have no conflicts of interest.

References

[1] M. Sugimoto, "The past, present, and future of ferrites," *Journal of the American Ceramic Society*, vol. 82, no. 2, pp. 269–280, 2004.

[2] T. Prakash, G. V. M. Williams, J. Kennedy, and S. Rubanov, "Formation of magnetic nanoparticles by low energy dual implantation of Ni and Fe into SiO2," *Journal of Alloys and Compounds*, vol. 667, pp. 255–261, 2016.

[3] Y. B. Kannan, R. Saravanan, N. Srinivasan, and I. Ismail, "Sintering effect on structural, magnetic and optical properties of Ni0. 5Zn0. 5Fe2O4 ferrite nano particles," *Journal of Magnetism and Magnetic Materials*, vol. 423, pp. 217–225, 2017.

[4] J. Kennedy, G. V. M. Williams, P. P. Murmu, and B. J. Ruck, "Intrinsic magnetic order and inhomogeneous transport in Gd-implanted zinc oxide," *Physical Review B*, vol. 88, no. 21, Article ID 214423, 2013.

[5] K. Jalaiah and K. Vijaya Babu, "Structural, magnetic and electrical properties of nickel doped Mn-Zn spinel ferrite synthesized by sol-gel method," *Journal of Magnetism and Magnetic Materials*, vol. 423, pp. 275–280, 2017.

[6] E. Kiani, A. S. H. Rozatian, and M. H. Yousefi, "Structural, magnetic and microwave absorption properties of SrFe12−2x(Mn0.5Cd0.5Zr)xO19 ferrite," *Journal of Magnetism and Magnetic Materials*, vol. 361, pp. 25–29, 2014.

[7] S. Abbas, M. Anis-ur-Rehman, and M. Anis-ur-Rehman, "Association of structural and enhanced transport properties in RE substituted cobalt nanoferrites," *Journal of Alloys and Compounds*, vol. 677, pp. 143–147, 2016.

[8] G. Aravind, M. Raghasudha, and D. Ravinder, "Electrical transport properties of nano crystalline Li–Ni ferrites," *Journal of Materiomics*, vol. 1, no. 4, pp. 348–356, 2015.

[9] S. Pande, M. M. Islam, S. C. Mohanta, and N. Uddin, "Single-step synthesis of manganese ferrite nanoparticles with enhanced magnetization via chemical co-precipitation route," *Journal of Scientific Research*, vol. 11, no. 2, pp. 225–234, 2019.

[10] R. Kumar, W. C. Macedo, R. K. Singh et al., "Nitrogen–sulfur co-doped reduced graphene oxide-nickel oxide nanoparticle composites for electromagnetic interference shielding," *ACS Applied Nano Materials*, vol. 2, no. 7, pp. 4626–4636, 2019.

[11] R. Kumar, S. Sahoo, E. Joanni, R. K. Singh, and K. K. Kar, "Microwave as a tool for synthesis of carbon-based electrodes for energy storage," *ACS Applied Materials & Interfaces*, vol. 14, no. 18, pp. 20306–20325, 2021.

[12] W. Liu, T. Yao, K. Jia, J. Gu, D. Wang, and X. Wei, "Flexible and thermal conducting multi-walled carbon nanotubes/waterborne polyurethane composite film from in situ polymerization for efficient electromagnetic interference shielding," *Journal of Materials Science: Materials in Electronics*, vol. 32, no. 4, pp. 4393–4403, 2021.

[13] N. Gulzar, K. Zubair, M. F. Shakir, M. Zahid, Y. Nawab, and Z. A. Rehan, "Effect on the EMI shielding properties of cobalt ferrites and coal-fly-ash based polymer nanocomposites," *Journal of Superconductivity and Novel Magnetism*, vol. 33, no. 11, pp. 3519–3524, 2020.

[14] R. Kumar, A. V. Alaferdov, R. K. Singh et al., "Self-assembled nanostructures of 3D hierarchical faceted-iron oxide containing vertical carbon nanotubes on reduced graphene oxide hybrids for enhanced electromagnetic interface shielding," *Composites Part B: Engineering*, vol. 168, pp. 66–76, 2019.

[15] Yi Hou, L. Cheng, Y. Zhang, X. Du, Y. Zhao, and Z. Yang, "High temperature electromagnetic interference shielding of lightweight and flexible ZrC/SiC nanofiber mats," *Chemical Engineering Journal*, vol. 404, Article ID 126521, 2021.

[16] C. H. Phan, M. Mariatti, and Y. H. Koh, "Electromagnetic interference shielding performance of epoxy composites filled with multiwalled carbon nanotubes/manganese zinc ferrite hybrid fillers," *Journal of Magnetism and Magnetic Materials*, vol. 401, pp. 472–478, 2016.

[17] P. Gairola, S. Gairola, V. Kumar, K. Singh, and S. Dhawan, "Barium ferrite and graphite integrated with polyaniline as effective shield against electromagnetic interference," *Synthetic Metals*, vol. 221, pp. 326–331, 2016.

[18] A. Kusiek, "Finite element/mode-matching analysis of ferrite/dielectric line junctions of arbitrary cross-section," *Journal of Electromagnetic Waves and Applications*, vol. 32, no. 1, pp. 67–76, 2018.

[19] M. Sabet, H. Jahangiri, and E. Ghashghaei, "Improving microwave absorption of the polyaniline by carbon nanotube and needle-like magnetic nanostructures," *Synthetic Metals*, vol. 224, pp. 18–26, 2017.

[20] R. Kumar, S. Sahoo, E. Joanni et al., "Recent progress on carbon-based composite materials for microwave electromagnetic interference shielding," *Carbon*, vol. 177, pp. 304–331, 2021.

[21] N. Devi, R. Kumar, S. Singh, and R. K. Singh, "Recent Development of Graphene-Based Composite for Multifunctional Applications: Energy, Environmental and Biomedical Sciences," *Critical Reviews in Solid State and Material Sciences*, vol. 47, 2022.

[22] K. Yoshizawa, So Noguchi, and H. Igarashi, "Influence of magnetic property of ferromagnetic shield on high field magnet analysis," *IEEE Transactions on Applied Superconductivity*, vol. 21, no. 3, pp. 2088–2091, 2011.

[23] S. Ren, S. Guo, X. Liu, and Q. Liu, "Shielding effectiveness of double-layer magnetic shield of current comparator under radial disturbing magnetic field," *IEEE Transactions on Magnetics*, vol. 52, no. 10, pp. 1–7, 2016.

[24] M. A. Almessiere, Y. Slimani, H. Güngüneş, A. Baykal, S. Trukhanov, and A. V. Trukhanov, "Manganese/yttrium codoped strontium nanohexaferrites: evaluation of magnetic susceptibility and mossbauer spectra," *Nanomaterials*, vol. 9, no. 1, p. 24, 2018.

[25] S. S. Bharambe, A. Trimukhe, and P. Bhatia, "Synthesis techniques of nickel substituted cobalt ferrites–an investigative study using structural data," *Materials Today Proceedings*, vol. 23, pp. 373–381, 2020.

[26] P. P. Hankare, K. R. Sanadi, K. M. Garadkar, D. R. Patil, and I. S. Mulla, "Synthesis and characterization of nickel substituted cobalt ferrite nanoparticles by sol–gel auto-combustion method," *Journal of Alloys and Compounds*, vol. 553, pp. 383–388, 2013.

[27] G. S. Kumar, T. Raguram, and K. S. Rajni, "Synthesis and characterization of nickel-substituted cobalt ferrite nanoparticles using sol–gel auto-combustion method," *Journal of Superconductivity and Novel Magnetism*, vol. 32, no. 6, pp. 1715–1723, 2019.

[28] K. Pubby, S. S. Meena, S. M. Yusuf, and S. Bindra Narang, "Cobalt substituted nickel ferrites via Pechini's sol–gel citrate route: X-band electromagnetic characterization," *Journal of Magnetism and Magnetic Materials*, vol. 466, pp. 430–445, 2018.

[29] A. R. Denton and N. W. Ashcroft, "Vegard's law," *Physical Review A*, vol. 43, no. 6, pp. 3161–3164, 1991.

[30] J. Sulaiman, S. M. Hamdoon, and G. Y. Abdulrahman, "Antibacterial activity of cobalt ferrite (CoFe2O4) nanoparticles against oral enterococci," in *Materials Science Forum*, vol. 1021, pp. 150–159, Trans Tech Publications Ltd, 2021.

[31] C. Pavlou, M. Giovanna, P. Carbone, and C. Anastasios, "Manikas, george trakakis, can koral, gianpaolo papari, antonello andreone, and costas galiotis. "Effective EMI shielding behaviour of thin graphene/PMMA nanolaminates in the THz range," *Nature Communications*, vol. 12, no. 1, pp. 1–9, 2021.

[32] A. Nairan, M. Khan, U. Khan, M. Iqbal, S. Riaz, and S. Naseem, "Temperature-dependent magnetic response of antiferromagnetic doping in cobalt ferrite nanostructures," *Nanomaterials*, vol. 6, no. 4, p. 73, 2016.

[33] B. Purnama and A. T. Wijayanta, "Effect of calcination temperature on structural and magnetic properties in cobalt ferrite nano particles," *Journal of King Saud University Science*, vol. 31, no. 4, pp. 956–960, 2019.

[34] S. N. Rafeeq, M. M. Ismail, and J. M. A. Sulaiman, "Magnetic and dielectric properties of $CoFe_2O_4$ and CoxZn1-xFe_2O_4 nanoparticles synthesized using sol-gel method," *Journal of Magnetics*, vol. 22, no. 3, pp. 406–413, 2017.

[35] A. Kumar and K. L. Yadav, "Magnetic, magnetocapacitance and dielectric properties of Cr doped bismuth ferrite nanoceramics," *Materials Science and Engineering: B*, vol. 176, no. 3, pp. 227–230, 2011.

[36] H. E. Hassan, T. Sharshar, M. M. Hessien, and O. M. Hemeda, "Effect of γ-rays irradiation on Mn–Ni ferrites: structure, magnetic properties and positron annihilation studies," *Nuclear Instruments and Methods in Physics Research Section B:*

Beam Interactions with Materials and Atoms, vol. 304, pp. 72–79, 2013.
[37] E. Sumalatha, D. Ravinder, N. Maramu et al., "Crystal chemistry, rietveld analysis, structural and electrical properties of cobalt-erbium nano-ferrites," *Ferrites: Synthesis and Applications*, vol. 17, 2021.
[38] R. Jabbar, S. H. Sabeeh, and A. M. Hameed, "Structural, dielectric and magnetic properties of Mn+ 2 doped cobalt ferrite nanoparticles," *Journal of Magnetism and Magnetic Materials*, vol. 494, Article ID 165726, 2020.
[39] A. S. Kakde, R. M. Belekar, G. C. Wakde, M. A. Borikar, K. G. Rewatkar, and B. A. Shingade, "Evidence of magnetic dilution due to unusual occupancy of zinc on B-site in NiFe2O4 spinel nano-ferrite," *Journal of Solid State Chemistry*, vol. 300, Article ID 122279, 2021.
[40] R. A. Young, "The rietveld method," *International Union of Crystallography*, vol. 5, pp. 1–38, 1993.
[41] J. R. Carvajal and J. Fullprof, "Fullprof: A program for Rietveld refinement and pattern matching analysis," *satellite meeting on powder diffraction of the XV congress of the IUCr*, vol. 127, 1990.
[42] J. R. Carvajal, "Short Reference Guide of the FullProf. Prog," *Laboratory Leon Brilloium (CEA-CNRS)*, 1997.
[43] B. Nandan, M. C. Bhatnagar, and S. C. Kashyap, "Cation distribution in nanocrystalline cobalt substituted nickel ferrites: X-ray diffraction and Raman spectroscopic investigations," *Journal of Physics and Chemistry of Solids*, vol. 129, pp. 298–306, 2019.
[44] K. Momma and F. Izumi, "VESTA 3 for three-dimensional visualization of crystal, volumetric and morphology data," *Journal of Applied Crystallography*, vol. 44, no. 6, pp. 1272–1276, 2011.
[45] S. M. Patange, S. E. Shirsath, S. P. Jadhav, V. S. Hogade, S. R. Kamble, and K. M. Jadhav, "Elastic properties of nanocrystalline aluminum substituted nickel ferrites prepared by co-precipitation method," *Journal of Molecular Structure*, vol. 1038, pp. 40–44, 2013.
[46] K. G. Kornev, D. Halverson, G. Korneva, Y. Gogotsi, and G. Friedman, "Magnetostatic interactions between carbon nanotubes filled with magnetic nanoparticles," *Applied Physics Letters*, vol. 92, no. 23, Article ID 233117, 2008.
[47] S. B. Narang, S. K. Chawla, R. K. Mudsainiyan, and K. Pubby, "Comparative dielectric analysis of Co-Zr doped M-type barium hexaferrites BaCoxZrxFe (12-2x) O19 prepared by different wet chemical routes," *Integrated Ferroelectrics*, vol. 167, no. 1, pp. 98–106, 2015.
[48] A. Rana, O. P. Thakur, and V. Kumar, "Effect of Gd3+ substitution on dielectric properties of nano cobalt ferrite," *Materials Letters*, vol. 65, no. 19-20, pp. 3191-3192, 2011.
[49] A. Baykal, İ. S. Ünver, U. Topal, and H. Sözeri, "Pb substituted Ba, Sr-hexaferrite nanoparticles as high-quality microwave absorbers," *Ceramics International*, vol. 43, no. 16, pp. 14023–14030, 2017.
[50] M. N. Ashiq, M. Javed Iqbal, and I. Hussain Gul, "Effect of Al–Cr doping on the structural, magnetic and dielectric properties of strontium hexaferrite nanomaterials," *Journal of Magnetism and Magnetic Materials*, vol. 323, no. 3-4, pp. 259–263, 2011.
[51] A. Arora and S. B. Narang, "Structural and dielectric properties of co-substituted M-type barium hexaferrite," *Journal of Materials Science: Materials in Electronics*, vol. 27, no. 10, pp. 10157–10162, 2016.
[52] M. Anis-ur-Rehman, S. Kanwal, Z. Khan, A. Asif, A. N. Hussain, and S. Zahid, "Study of dielectric relaxations in co-precipitated Sr–Fe(Cr) nanoferrites," *Journal of Materials Science: Materials in Electronics*, vol. 26, no. 9, pp. 6539–6545, 2015.
[53] M. J. Iqbal, M. N. Ashiq, P. Hernández-Gómez, J. M. M. Muñoz, and C. T. Cabrera, "Influence of annealing temperature and doping rate on the magnetic properties of Zr–Mn substituted Sr-hexaferrite nanoparticles," *Journal of Alloys and Compounds*, vol. 500, no. 1, pp. 113–116, 2010.
[54] Y. Shi, J. Ding, and H. Yin, "CoFe2O4 nanoparticles prepared by the mechanochemical method," *Journal of Alloys and Compounds*, vol. 308, no. 1-2, pp. 290–295, 2000.
[55] F. Kools and R. Henket, "The effect of A1203 substitution on the microstructure and coercivity of polycrystalline SrFel2Ot9," *Proceedings ICF*, vol. 5, pp. 417–421, 1989.
[56] J. M. A. Sulaiman, M. M. Ismail, S. N. Rafeeq, and A. Mandal, "Enhancement of electromagnetic interference shielding based on Co0. 5Zn0. 5Fe2O4/PANI-PTSA nanocomposites," *Applied Physics A*, vol. 126, no. 3, pp. 236–239, 2020.
[57] M. Mozaffari, J. Amighian, and E. Darsheshdar, "Magnetic and structural studies of nickel-substituted cobalt ferrite nanoparticles, synthesized by the sol–gel method," *Journal of Magnetism and Magnetic Materials*, vol. 350, pp. 19–22, 2014.
[58] N. B. Velhal, N. D. Patil, A. R. Shelke, N. G. Deshpande, and V. R. Puri, "Structural, dielectric and magnetic properties of nickel substituted cobalt ferrite nanoparticles: effect of nickel concentration," *AIP Advances*, vol. 5, no. 9, Article ID 097166, 2015.
[59] Ru Zhang, Li Sun, Z. Wang, W. Hao, E. Cao, and Y. Zhang, "Dielectric and magnetic properties of CoFe2O4 prepared by sol-gel auto-combustion method," *Materials Research Bulletin*, vol. 98, pp. 133–138, 2018.
[60] S. Singhal, J. Singh, S. K. Barthwal, and K. Chandra, "Preparation and characterization of nanosize nickel-substituted cobalt ferrites (Co1− xNixFe2O4)," *Journal of Solid State Chemistry*, vol. 178, no. 10, pp. 3183–3189, 2005.
[61] Z.-li Lu, P.-zhao Gao, R.-xue Ma, J. Xu, Z.-he Wang, and E. V. Rebrov, "Structural, magnetic and thermal properties of one-dimensional CoFe2O4 microtubes," *Journal of Alloys and Compounds*, vol. 665, pp. 428–434, 2016.
[62] M. Molazemi, H. Shokrollahi, and B. Hashemi, "The investigation of the compression and tension behavior of the cobalt ferrite magnetorheological fluids synthesized by co-precipitation," *Journal of Magnetism and Magnetic Materials*, vol. 346, pp. 107–112, 2013.
[63] J. Jiang, Y.-M. Yang, and L.-C. Li, "Effect of heat treatment on the magnetic properties of nanocrystalline spinel Li–Ni ferrite prepared by a simple soft chemistry route," *Journal of Alloys and Compounds*, vol. 464, no. 1-2, pp. 370–373, 2008.
[64] P. Gao, X. Hua, V. Degirmenci et al., "Structural and magnetic properties of Ni1− xZnxFe2O4 (x= 0, 0.5 and 1) nanopowders prepared by sol–gel method," *Journal of Magnetism and Magnetic Materials*, vol. 348, pp. 44–50, 2013.
[65] K. M. Srinivasamurthy, V. Angadi, S. P. Kubrin, S. Matteppanavar, P. M. Kumar, and B. Rudraswamy, "Evidence of enhanced ferromagnetic nature and hyperfine interaction studies of Ce-Sm doped Co-Ni ferrite nanoparticles for microphone applications," *Ceramics International*, vol. 44, no. 15, pp. 18878–18885, 2018.
[66] G. K. Joshi, A. Y. Khot, and S. R. Sawant, "Magnetisation, curie temperature and Y- K angle studies of Cu substituted and non substituted Ni- Zn mixed ferrites," *Solid State Communications*, vol. 65, no. 12, pp. 1593–1595, 1988.
[67] Y. Yafet and C. Kittel, "Antiferromagnetic arrangements in ferrites," *Physical Review*, vol. 87, no. 2, pp. 290–294, 1952.

[68] A. R. Kagdi, N. P. Solanki, F. E. Carvalho et al., "Influence of Mg substitution on structural, magnetic and dielectric properties of X-type bariumzinc hexaferrites Ba2Zn2-xMgxFe28O46," *Journal of Alloys and Compounds*, vol. 741, pp. 377–391, 2018.

[69] A. Saboor, A. N. Khan, H. M. Cheema, K. Yaqoob, and A. Shafqat, "Effect of polyaniline on the dielectric and EMI shielding behaviors of styrene acrylonitrile," *Journal of Materials Science: Materials in Electronics*, vol. 27, no. 9, pp. 9634–9641, 2016.

[70] R. Anum, M. Zahid, S. Siddique, H. M. F. Shakir, and Z. A. Rehan, "PVC based flexible nanocomposites with the incorporation of Polyaniline and Barium Hexa-Ferrite nanoparticles for the shielding against EMI, NIR, and thermal imaging cameras," *Synthetic Metals*, vol. 277, Article ID 116773, 2021.

[71] S. Siddique, M. Zahid, R. Anum, H. M. F. Shakir, and Z. A. Rehan, "Fabrication and characterization of PVC based flexible nanocomposites for the shielding against EMI, NIR, and thermal imaging signals," *Results in Physics*, vol. 24, Article ID 104183, 2021.

[72] M. F. Shakir, A. N. Khan, R. Khan et al., "EMI shielding properties of polymer blends with inclusion of graphene nano platelets," *Results in Physics*, vol. 14, Article ID 102365, 2019.

[73] K. Pubby and S. Bindra Narang, "Ka band absorption properties of substituted nickel spinel ferrites: Comparison of open-circuit approach and short-circuit approach," *Ceramics International*, vol. 45, no. 17, pp. 23673–23680, 2019.

[74] N. Song, S. Gu, Q. Wu et al., "Facile synthesis and high-frequency performance of CoFe2O4 nanocubes with different size," *Journal of Magnetism and Magnetic Materials*, vol. 451, pp. 793–798, 2018.

[75] M. M. Ismail, S. N. Rafeeq, J. M. A. Sulaiman, and A. Mandal, "Electromagnetic interference shielding and microwave absorption properties of cobalt ferrite CoFe2O4/polyaniline composite," *Applied Physics A*, vol. 124, no. 5, pp. 1–12, 2018.

[76] F. Movassagh-Alanagh, A. Bordbar-Khiabani, and A. Ahangari-Asl, "Three-phase PANI@ nano-Fe3O4@ CFs heterostructure: fabrication, characterization and investigation of microwave absorption and EMI shielding of PANI@ nano-Fe3O4@ CFs/epoxy hybrid composite," *Composites Science and Technology*, vol. 150, pp. 65–78, 2017.

[77] D. Wanasinghe and F. Aslani, "A review on recent advancement of electromagnetic interference shielding novel metallic materials and processes," *Composites Part B: Engineering*, vol. 176, Article ID 107207, 2019.

[78] K. Zubair and M. F. Shakir, "Effect of polymer matrix in polymer/trGO nano-composite for EMI shielding application in microwave and infrared region," in *Key Engineering Materials*, vol. 875, pp. 153–159, Trans Tech Publications Ltd, 2021.

[79] A. K. Singh, A. Shishkin, T. Koppel, and N. Gupta, "A review of porous lightweight composite materials for electromagnetic interference shielding," *Composites Part B: Engineering*, vol. 149, pp. 188–197, 2018.

[80] M. Gholampoor, F. Movassagh-Alanagh, and H. Salimkhani, "Fabrication of nano-Fe3O4 3D structure on carbon fibers as a microwave absorber and EMI shielding composite by modified EPD method," *Solid State Sciences*, vol. 64, pp. 51–61, 2017.

[81] H. Y. Liu and Y. S. Li, "Synthesis and microwave absorbing properties of cobalt ferrite IOP conference series: materials science and engineering," *IOP Conference Series: Materials Science and Engineering*, vol. 292, no. 1, Article ID 012062, 2018.

[82] K. Zubair, M. F. Shakir, A. Afzal, Z. A. Rehan, and Y. Nawab, "Effect of barium hexaferrites and thermally reduced graphene oxide on EMI shielding properties in polymer composites," *Journal of Superconductivity and Novel Magnetism*, vol. 34, no. 1, pp. 201–210, 2021.

[83] N. Aggarwal and S. B. Narang, "Effect of co-substitution of Co–Zr on electromagnetic properties of Ni–Zn spinel ferrites at microwave frequencies," *Journal of Alloys and Compounds*, vol. 866, Article ID 157461, 2021.

[84] K. Praveena and M. Bououdina, "Tunable microwave absorbing properties of CoFe2O4/PANI nanocomposites," *Journal of Electronic Materials*, vol. 49, no. 10, pp. 6187–6198, 2020.

[85] A. N. Hapishah, M. M. Syazwan, and M. N. Hamidon, "Synthesis and characterization of magnetic and microwave absorbing properties in polycrystalline cobalt zinc ferrite (Co0. 5Zn0. 5Fe2O4) composite," *Journal of Materials Science: Materials in Electronics*, vol. 29, no. 24, pp. 20573–20579, 2018.